九州大学学術情報リポジトリ
Kyushu University Institutional Repository

Numerical analysis and modeling of non-spherical particle’s motion

張, 煒

https://doi.org/10.15017/1866292

出版情報：Kyushu University, 2017, 博士（工学）, 課程博士
バージョン：
権利関係：

GRADUATE SCHOOL OF ENGINEERING

KYUSHU UNIVERSITY

Department of Mechanical Engineering

Doctoral Dissertation

Numerical analysis and modeling of non-spherical particle's motion

(非球形粒子運動の数値解析及びモデリング)

June 29, 2017

Supervisor: Prof. Dr. KITGAWA Toshiaki

Supervisor: Assoc. Prof. Dr. WATANABE Hiroaki

Student ID: 3TE14095P

ZHANG WEI

Abstract

This dissertation mainly investigates the behavior of the non-spherical particles. Firstly, a new spheroidal particle motion model is proposed based on the numerical simulation of six degrees of freedom motion of a single spheroidal particle. This model uses a sine curve's probability density function (PDF) to represent the particle's rotation. Secondly, the spheroidal particle motion model is introduced into a numerical code to simulate the particles' dispersion in an isotropic turbulence flow. The differences between the spherical and the spheroidal model are discussed by the statistical methods and the results are organized in terms of the Stokes number. Next, an experiment and a simulation of particles' dispersion of a real scale jet burner are performed. In the experiment, pulverized coal and spherical polymer particles are used, while in the simulation the spherical and spheroidal particles with and without diameter distribution are used. The simulation results are compared with the experimental results. The particle's shape effect and diameter distribution effect are discussed. Finally, in order to investigate a single particle's ignition behavior, a simulation of a single particle freely moving in a vertical uniform flow with devolatilization is performed. The Extended-CPD (extended chemical percolation devolatilization) model is applied to calculate the volatile velocity. The results are examined and discussed by applying the Flame Index.

Key words: Particle shape effect, Jet-burner, Isotropic turbulence flow, Particle dispersion, Ignition

Contents

List of Figures **iii**

List of Tables **vi**

Symbols & Abbreviation **vii**

1 Introduction **1**

1.1 Background 1

1.1.1 The role of the coal in the world 1

1.1.2 IGCC power generation 2

1.1.3 Problems 4

1.2 Purpose and contents of this dissertation 6

2 Modeling of a spheroidal particle's motion **8**

2.1 Particle's motion 8

2.2 Single spheroidal particle motion 10

2.3 Spheroidal particle motion model 13

3 Particle's shape effect on particle dispersion in an isotropic turbulence flow **15**

3.1 Introduction 15

3.2 Governing equations 17

3.3 Statistical method for the evaluation of the particles' dispersion 17

3.3.1 D number method 18

3.3.2 RDF method 19

3.4 Computational details 20
3.5 Results and discussion 22
3.5.1 Results of D number method 23
3.5.2 Results of RDF method 27
3.6 Chapter conclusion 30

4 Particle's shape effect on particle dispersion in a jet flow 31
4.1 Introduction 31
4.2 Experimental details 32
4.3 Numerical methods 33
4.3.1 Governing equations 33
4.3.2 Evaluation of particle number intensity 34
4.4 Computational details 35
4.5 Results and discussion 37
4.5.1 Velocity profile 37
4.5.2 The particle dispersion 45
4.5.3 RDF analysis of the particle distribution 51
4.6 Chapter conclusions 53

5 A single non-spherical particle's ignition in a vertical uniform flow 54
5.1 Introduction 54
5.2 Numerical methods 56
5.2.1 Governing equations 56
5.2.2 Chemical reaction modeling 58
5.2.3 Flame index 59
5.3 Computational details 59
5.4 Results and discussion 62
5.4.1 Particle surface temperature and volatile velocity 62
5.4.2 Comparing with experimental result 64
5.4.3 Mixture gas formation before ignition 67

5.4.4 Ignition behavior 69
5.5 Chapter conclusions 72

6 Conclusions and suggestions **77**
6.1 Conclusion of the dissertation 77
6.2 Directions for future works 79

References **79**

Acknowledgment **83**

List of Figures

1.1 A common configuration of an IGCC system. 2

1.2 The IGCC system with CO_2 capture. 3

2.1 Typical computational grid. 11

2.2 Shapes of the spheroid particle. 11

2.3 Drag curves for EV00, EV30, EV60 and EV90. “MIN” is obtained by the motion of non-rotation(fixed) EV90 particle. 13

2.4 PDF of C_D for (a) EV30, (b) EV60 and (c) EV90, including the PDF of a sine curve. The values on the horizontal axis are normalized by the maximum and minimum C_D values for each case. 0 represents the minimum and 1 represents the maximum. 13

3.1 The schematic view of the D number method. 18

3.2 The schematic view of the RDF calculation. 20

3.3 Visualization of the vortex defined by $Q_2 = 10000$ for SV. 23

3.4 Drag coefficient of a spheroid and its PDF curve. 24

3.5 Variations in the D number and the Stk number in the calculation of ES85. 25

3.6 Comparison of the D number by case. 25

3.7 (a) Comparison of the C_D curves between SV, EL90 and EL85. (b) Comparison of the C_D curves between SV andEL96. 28

3.8 RDF results at four certain Stk numbers. 29

3.9 Sum of $g(r)$ values while $r/\eta < 12$ for each case. 29

4.1 The schematic design of the experiment configuration. 32

4.2 A look of the experiment. 33
4.3 The procedure to calculate the particle number intensity. 35
4.4 By average various instantaneous particle number intensity figures, we finally get a averaged Mie scattering look-like result. 36
4.5 The particle mass flux rate of different diameters. 37
4.6 Calculation domain of the simulation. 38
4.7 Averaged vertical velocity at different height for all the cases. 40
4.8 Standard deviation of the vertical velocity at different height for all cases. 41
4.9 Averaged radial velocity at different height for all the cases. 43
4.10 Standard deviation of the radial velocity at different height for all cases. . 44
4.11 Mie scattering of the experiment and the particle number intensity of the simulation at instant. 46
4.12 Time averaged Mie scattering of the experiment and the particle number intensity of the simulation. 48
4.13 The width measured at different heights. 49
4.14 Averaged Mie scattering intensity of the experiment and the number intensity of the simulation at different height. 50
4.15 The RDF results at each height. 52

5.1 Schematic of simulation. 60
5.2 Calculation domain and particle shape. 60
5.3 Six tracking points are chosen. 62
5.4 The temperature variation of the six tracking points. 65
5.5 The volatile velocity of the six tracking points. 65
5.6 The ignition delay of the experimental. The diamond mark represents the simulation result. 66
5.7 The flame inclined angle of the experimental and simulation data. The velocity ratio in the experiment is the ratio between the particle carrier gas and the hot flow. The diamond mark represents the simulation result. . 67

5.8 The premixed region and diffusion region identified by FI. Green area is FI = 0. 69
5.9 The premixed region and diffusion region identified by FI and corresponding temperature distribution. Green area and black line represent FI = 0. . 70
5.10 The premixed flame and diffusion flame identified by FI before 4ms. Green area is FI = 0. 73
5.11 The premixed flame and diffusion flame identified by FI after 4ms. Green area is FI = 0. 74
5.12 The concentration variation of methane and oxygen. Temperature is also shown in it. (a) shows the white line where the data sampled. The sample line length is 2 mm, particle is located at the center, thus the points at 1 mm do not have data. 75

List of Tables

2.1 Properties in all cases. 12

3.1 Particle properties used in the $C_D - Re$ equations. 21

3.2 Parameters A, B, C, X, Y used in each case. 22

4.1 The cases performed in the experiment. 32

4.2 The cases performed in the simulation. 36

5.1 The property of the spheroidal particle used in this chapter. 61

5.2 The parameters needed for the Extend-CPD model. Here the unit of NMR analysis indicates how many chemical bonds in one mole bonds. Ar represents the aromatic ring. 63

Symbols & Abbreviation

F_D	:	Drag force
C_D	:	Drag coefficient
C_{Dmax}	:	Maximum drag coefficient
C_{Dmin}	:	Minimum drag coefficient
C_L	:	Lift coefficient
Re	:	Reynolds number
Stk	:	Stokes number
Φ	:	Sphericity
Q_2	:	The second invariant of the velocity gradient tensor
η	:	Kolmogorov length scale
τ_p	:	Particle response time
D	:	The D number used to identify particle clustering
θ	:	Random number to represent particle's rotation in spheroidal motion model
A, B, C, X, Y	:	Five parameters used in the spheroidal particle motion model

ALE	:	Arbitrary Lagrangian-Eulerian method
PDF	:	Probability density function
RDF	:	Radial distribution function
PIV	:	Particle image velocimetry
SD	:	Standard deviation
FI	:	Flame index

CHAPTER 1

Introduction

1.1 Background

1.1.1 The role of the coal in the world

In the world, the consumption of the primary energy is increasing year by year. According to the annual report from the U.S. Energy Information Administration (EIA), the energy consumption in 2040 will rise to 1.5 times compared to 2012 [1]. Most of this increase come from the emerging developing economies mainly located in Asia, like China and India. These emerging economies, which have achieved great economic development in recent years, are expected to have an accelerated growth in the future. Along with this, the demand for fossil fuels such as petroleum, coal and natural gas which supporting the economy are expected to have a great increase.

However, the reserves of the fossil fuels are limited. According to the report from the BP Global, the remaining lifetime of the fossil fuels are 51 years for petroleum, 53 years for natural gas, and about 114 years for coal, respectively [2]. These numbers may change due to the discovery of new oil fields and mines, and technological innovation on the energy use. It is still a “limited resource” for the fossil fuels that they will run out someday. Compared to the coal, the petroleum and natural gas are unevenly distributed in the world and have a shorter lifetime. Most of the oil fields exist in the Middle East, where is in the unstable political situation. This leads to a risk of the oil supply and an unstable crude oil price. And since the emerging economies developing, it is considered

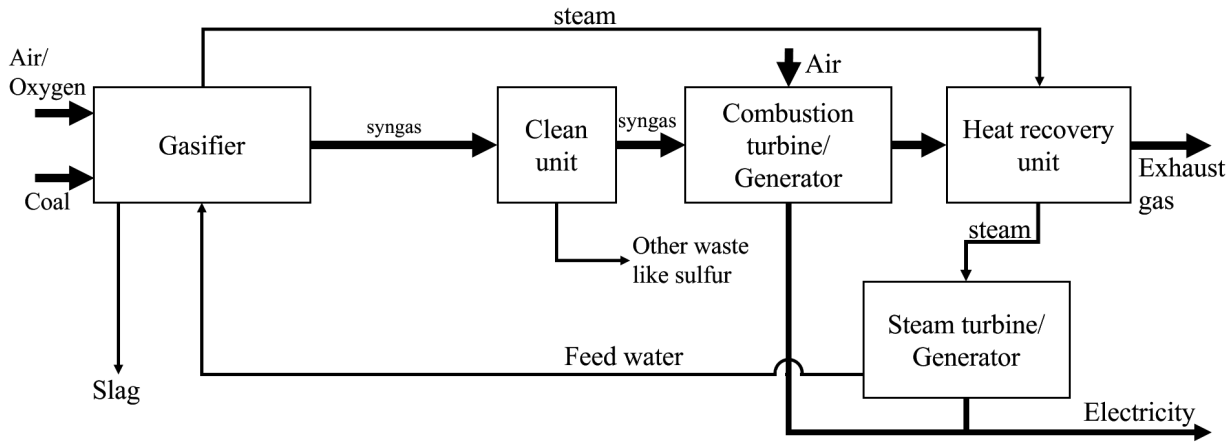

Figure 1.1: A common configuration of an IGCC system.

the demand of the oil will rapidly increase, causing a rising oil price. On the contrast, the coal is widely distributed in the world and have a longer lifetime, almost twice than the crude oil. It has a cheap and stable price, and its supply is also reliable. These merits make the coal the most important primary energy in the world. The coal is mainly utilized in the power production. The coal-fired power plant responded for 36% of the electricity around the world [3]. Thus the coal is exactly an "indispensable" energy source.

Nevertheless, the coal has a high CO_2 emission intensity, that makes a greater contribution to the global warming. In the future, the energy demand of emerging countries will soar and the consumption of the coal will increase accordingly. Hence there is an urgent need to realize a clean coal technology to reduce the CO_2 emission.

1.1.2 IGCC power generation

Integrated gasification combined cycle (IGCC) is a technology that attracts the attention of the world. It integrates the coal gasification system and the combined cycle power generation system. It utilizes the coal or other carbon-based fuels in a high-pressure gasifier, and turns them into pressurized syngas which is composed of CO and H_2. After then, the syngas passes a purification process includes the dust removal, mercury removal, sulfur removal and so on. Finally, the clean syngas is passed to the combined cycle to produce electricity. Figure 1.1 shows the common configuration of an IGCC system.

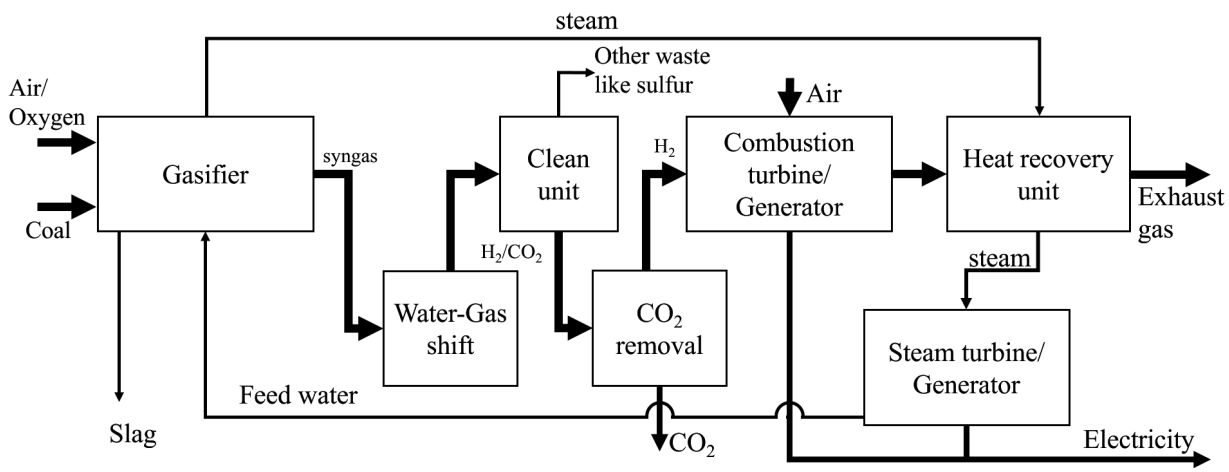

Figure 1.2: The IGCC system with CO_2 capture.

Due to the particular power generation pattern, the IGCC system has many benefits. It needs less water compared with the same scale pulverized coal power plant. Since in the IGCC, the power is mainly generated by the combustion turbine, which needs less water than the steam turbine. This is a very important advantage that enables to build a power plant in a water-lack region. The IGCC system's wastes can be used to produce other industrial product. Like the slag from the coal gasifier and fines from the electrostatic precipitators can be used to produce cement and asphalt joint filler. The sulfur from the sulfur removal can be used to produce pure sulfur. The biggest advantage is that the IGCC system can be easily coupled with the CO_2 capture and storage (CCS) technology, shown in Figure 1.2. This is because that in the IGCC system, the coal has been turned into the syngas of CO and H_2, and the syngas can be easily turned into a composition of CO_2 and H_2 through a water-gas shift process. Then the CO_2 can be removed and compressed for storage. This is estimated to have a lower cost than the pulverized coal with CO_2 capture.

In a whole IGCC system, the coal gasifier and the purification system of the syngas determine whether the IGCC system can be commercialized or not. The syngas production rate, syngas heat value, operation pressure and temperature of the coal gasifier must satisfy the design requirements. The coal gasifier must have a better load regulation performance, which satisfies the load regulation requirement of the power plant. The composition of the production of the coal gasifier must satisfy the load regulation require-

ment of the combined cycle system. The coal gasifier must have a wide applicability of a variety of coals. And finally, the coal gasifier must be simple, reliable, easy to be operated and maintained.

Although the requirements of the coal gasifier are not easy to be achieved, the IGCC system is the leading candidate for the electricity production with CO_2 capture at present.

1.1.3 Problems

All of the requirements of the coal gasifier indicate that the designer of the coal gasifier must have a deep understanding inside the gasifier. This means we must interpret the complex phenomenon of the solid-gas multiphase flow inside the gasifier. Including the simultaneous and interactive coal particle dispersion, coal evaporation, and devolatilization of pulverized coal particles, as well as the heterogeneous and homogeneous reactions of the gas phase. These phenomena are such complex and happen inside the gasifier with extremely high pressure and temperature that they are very hard to be observed directly. Hence we do not achieve a deep understanding of the coal gasification phenomenon in the coal gasifier yet.

In order to solve the problem, the Computational Fluid Dynamics (CFD) is applied. Through the simulations of the solid-gas flow inside the gasifier, we obtain the rough image of the coal gasification. However, because of the limit of the computer ability and the model accuracy, a simulation of the real scale of the gasifier with high accuracy can not be performed.

Generally, in a multiphase CFD, the shape of the solid particle is assumed to be spherical to reduce computational cost. Since the complex shape effect is neglected, the simulation accuracy of the particle's motion can not be guaranteed. According to the research of Elghobashi [4], the solid-gas two-phase flow can be divided into two types, dilute suspension and dense suspension, in terms of the volume fraction of particles. In the dense suspension, since the particles' volume fraction is high, the collision of the particle to particle takes place. This affects the particles' motion significantly. However, in the dilute suspension, due to the low volume fraction of particles, the collisions between particles

happens rarely and negligible. Thus other factors, such as shape effect, affect the particles' motion greatly. In the future, it is envisioned that as the IGCC system becomes practical, the system will become more large-scaled. Inside a coal gasifier, the dilute suspension cases will become more and more. Therefore, the spherical particle assumption may not reproduce the particle's motion inside a gasifier accurately. The particle's shape effect on particle's motion shall be taken into account to improve the precision of numerical simulations.

And another, for a single particle, the particle ignition procedure has not been revealed yet. There are rare researchers discussed these problems and evaluate the particle's shape effect on the particle's motion and ignition behavior in the past.

1.2 Purpose and contents of this dissertation

As above sections shows, most solid-gas two-phase simulations neglects the particles' real shapes and assume them to be spherical. The particle's shape effect in numerical simulations has rarely been discussed. This dissertation mainly focuses on the particle shape affects. It tries to represent a pulverized coal particles using spheroidal particles. For example, for the coal particles have nearly spherical shape, the spheroidal particles which have close major and minor radius can be used. Conversely, for the coal particles have extremely strange shapes, such as long and thin particles, the prolate spheroidal particles can be used. In order to achieve the purpose, the single spheroidal particle's motion is investigated and modeled. Then it discusses the spherical and spheroidal particle's dispersion behavior in the isotropic and jet-burner flow. The contents of this dissertation consist of the chapters below.

In chapter two, it gives the modeling of a spheroidal particle's motion. This model is applied to the simulation later and is compared to the widely-used spherical model.

In chapter three, the simulation of the particles' dispersion in an isotropic turbulence flow is performed. The spherical and spheroidal particle motion model are applied. The results are analyzed by using statistical methods. The difference between the spherical and the spheroidal particles' dispersion is discussed.

In chapter four, both an experiment and a simulation of the particles' dispersion of a jet flow are performed. In experiment cases, pulverized coal and spherical polymer particles are used. In simulation cases, the spherical and spheroidal particle motion model are applied. The simulation results are compared to the experimental data to discuss the shape effect and the diameter distribution effect.

In chapter five, it discusses the simulation of a single spheroidal particle's ignition in a vertical uniform flow. The Extended-CPD model is introduced to calculate the volatile velocity on the particle surface. With this model, the particle's volatile velocity is calculated in terms of the particle composition and the temperature distribution over the surface. The

global reaction is applied for the gas reaction. The particle's ignition behavior is discussed by tracking the Flame Index.

In chapter six, it summarizes the conclusions of this dissertation and suggests the future work.

CHAPTER 2

Modeling of a spheroidal particle's motion

2.1 Particle's motion

For a particle moving in a fluid, both of the translation and rotation shall be considered. For a spherical particle, since it has a completely symmetrical shape, its rotation is neglected, and only the translation term remained. The well-known Basset-Boussinesq-Oseen equation (B.B.O equation), which is valid for a spherical particle moving in a fluid, is expressed as

$$\rho_p V_p \frac{d\boldsymbol{v}}{dt} = \boldsymbol{F}_D + \boldsymbol{F}_L + \boldsymbol{F}_B + \boldsymbol{F}_{prs} + \boldsymbol{F}_{mass} + \boldsymbol{F}_{Basset}, \tag{2.1}$$

where ρ_p, V_p and $\boldsymbol{v}$ are the density, volume, and velocity of the particle, respectively. $\boldsymbol{F}_D$, $\boldsymbol{F}_L$, $\boldsymbol{F}_B$, $\boldsymbol{F}_{pre}$, $\boldsymbol{F}_{mass}$, and $\boldsymbol{F}_{Basset}$ are the drag force, lift force, buoyancy, pressure gradient, virtual mass, and Basset history term, respectively. Because the drag force mainly contributes to the motion of a particle in a pulverized coal combustion field, this study pays special attention to it. The drag force can be calculated by summing the contributions of friction and pressure as

$$\boldsymbol{F}_D = \boldsymbol{F}_{Dprs} + \boldsymbol{F}_{Dfrc} = -\int_S p\boldsymbol{e}_y \cdot \boldsymbol{n} dS + \int_S \boldsymbol{n} \cdot \tau \cdot \boldsymbol{e}_y dS, \tag{2.2}$$

where $\boldsymbol{n}$ is the surface normal vector, τ is the stress tensor, and $\boldsymbol{e}_y$ is the particle's direction

of motion. Although Equation (2.2) can be used for any particle, Equation (2.1) is only strictly valid for spheres.

The drag coefficient C_D is defined as

$$C_D = \frac{\boldsymbol{F}_D}{\frac{1}{2}\rho_f(\boldsymbol{u}-\boldsymbol{v})^2 A} = C_{Dprs} + C_{Dfrc}, \tag{2.3}$$

where ρ_f and $\boldsymbol{u}$ are the fluid density and velocity, respectively. A is the projection area of the particle to the flow direction. C_D can also be divided into C_{Dprs} and C_{Dfrc}, which are influenced by the friction and the pressure, respectively. Clift *et al*. summarized some of the most popular expressions [5, p. 111] and provided the following recommendation

$$\begin{aligned} C_D &= 3/16 + 24/Re, & Re < 0.01 \quad &(2.4a)\\ &= \frac{24}{Re}(1 + 0.1315 Re^{0.82-0.05*\log_{10} Re}), & 0.01 < Re \leq 20 \quad &(2.4b)\\ &= \frac{24}{Re}(1 + 0.1935 Re^{0.6305}). & 20 \leq Re < 260 \quad &(2.4c) \end{aligned}$$

Where the Re is the particle Reynolds number, defined as

$$Re = \frac{\rho_f(\boldsymbol{u}-\boldsymbol{v})d}{\mu} \tag{2.5}$$

here d is the diameter of the particle and μ is the fluid viscosity.

However, Equations (2.1) and (2.4) are only suitable for spherical particles. These equations must be modified for non-spherical particles. Haider & Levenspiel [6] studied C_D of non-spherical particles by investigating the relations between C_D, Re and sphericity. They proposed a design chart of C_D with the sphericity dependence.

Sphericity is defined as the ratio of the surface area of a sphere to the surface area of a given particle where the sphere and the given particle have same volume as

$$\phi = \frac{S_{sphere}}{S_{particle}} = \frac{\pi^{\frac{1}{3}}(6V_{particle})^{\frac{2}{3}}}{S_{particle}}. \tag{2.6}$$

According to their conclusions, C_D becomes larger as the sphericity becomes smaller. However, the effect of rotation and oscillation of the particle cannot be considered in their formula because the modified C_D expresses the equivalent diameter of a spherical particle.

2.2 Single spheroidal particle motion

As above section mentioned, the particle's motion mainly depends on the drag coefficient C_D. Hence in order to build a non-spherical particle motion model, the single non-spherical particle's motion behavior shall be observed to modify the $C_D - Re$ equation such as Equation (2.4).

In previous researches, a numerical simulation with six degrees of freedom motion of a single spherical or spheroidal particle was performed by employing the Arbitrary Lagrangian-Eulerian (ALE) method to numerically investigate the particle's behavior in terms of the drag coefficient curve [7]. The ALE method was firstly validated by calculating a spherical particle's C_D values and compared them to the empirical Equation (2.4). Secondly the method was validated by comparing the simulations with the experiment by Mordant & Pinton [8], in which the velocity of different materials settling in resting water was measured. It shown that the results of the spherical particle agreed well with the Equation (2.4) in the first validation, and captured the vortex shedding behavior accurately in the second validation.

After then, the ALE method was applied to investigate the motion of a particle entrained in an upward uniform flow. The flow was upward and its velocity was set to $\boldsymbol{u} = 15$m/s. The particle was placed in the upward flow at the beginning of the computation. The particle was released at $t = 0$ without an initial velocity. After releasing, the particle was moving in the flow freely. The initial particle Reynolds number was about $Re \approx 45$. This was the condition generally observed in a pulverized coal combustion system.

The particle with spheroidal shape was examined. The size of the particle was determined by the typical pulverized coal particle size. Its sphericity was set to 0.96 and the minor axis length was calculated accordingly. Totally four cases were examined. Table 2.1 listed the cases while Figure 2.1 shown the computational grid of EV90. All the cases used the same spheroidal particle, but different initial orientations. The initial orientation was the angle between the spheroid's major axis and the horizontal plane. Since the flow

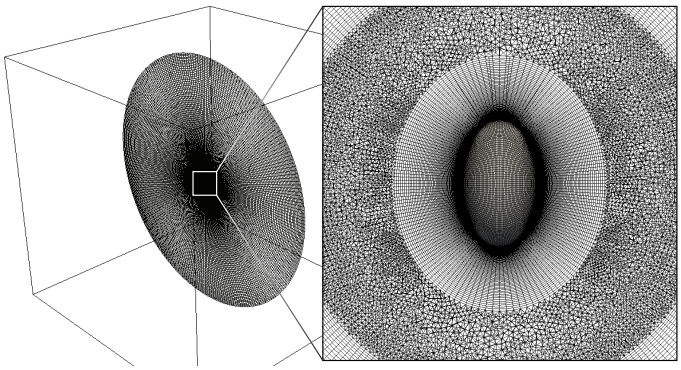

Figure 2.1: Typical computational grid.

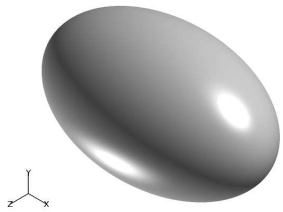

Figure 2.2: Shapes of the spheroid particle.

was upward, an initial orientation of 0° meant the particle's major axis was perpendicular to the flow direction, and an initial orientation of 90° meant the particle's major axis was along the flow direction. In this chapter, the initial orientations were from 0° to 90° with an interval of 30°. As previously mentioned, the boundary condition for the velocity field surrounding the computational domain was fixed as a uniform flow.

Figure 2.3 shows the C_D curves of the results of all the spheroid cases. In this figure, "MIN" is the lower limit shown by the motion of the spheroid with a compulsorily fixed vertical orientation. The EV00's C_D curve is smooth, and similar to that of the sphere and shows the upper limit, because the spheroid with the horizontal initial orientation is in a stable state with the largest projection area in the flow direction. The C_D curves oscillate between the lower and upper limits for the other initial orientations. The oscillation of the C_D curve is highly dependent on the particle's rotation motion. Although all the cases have the same particle shape, since the initial orientations are different, the oscillation characteristics of the C_D curves differ. Its behavior depends not only on the instantaneous *Re* number but also on the balance between the inertia momentum and the fluid force

Table 2.1: Properties in all cases.

Case	Shape	$D1^*$	$D2^*$	$D3^*$	initial orientation**	sphericity
EV00	Figure 2.2	60	35	35	0°	0.96
EV30					30°	
EV60					60°	
EV90					90°	

* Diameter with unit μm. All adjusted to the coal particle, for which the characteristic length is measured by its circumscribed circle from the X, Y, and Z direction.

** Initial orientation is the angle between the spheroid's major axis and the horizontal plane. Since the flow is upward, an initial orientation of 0° means the particle's major axis is perpendicular to the flow direction, and an initial orientation of 90° means the particle's major axis is along the flow direction.

acting on the particle.

Figure 2.4 shows the probability density function (PDF) of the C_D values for EV30, EV60, and EV90. The values on the horizontal axis are normalized by the maximum and minimum C_D values for each case. 0 represents the minimum C_D value, while 1 represents the maximum C_D value. For EV90, C_D is always oscillating between the maximum and the minimum values. On the other hand, four spikes at 0.19, 0.49, 0.59, and 0.71 for EV30, one spike at 0.13 for EV60 appears. It is considered that the number of spikes corresponds to the count of the particle's oscillations. For example, for EV60 after releasing, the particle oscillates only once and then starts to rotate. This indicates that as the particle is entrained, the *Re* number decreases, and the fluid force acting on the particle becomes smaller and is insufficient to provide the momentum to change the particle's oscillation direction. Hence, the oscillation mode, which is like a seesaw, changes into the rotation mode. For EV30, the fluid force acting toward the counter-rotating direction is larger than the rotating inertia force and the particle changes its direction of oscillation four times. As the slip velocity becomes smaller, the momentum provided from the slip

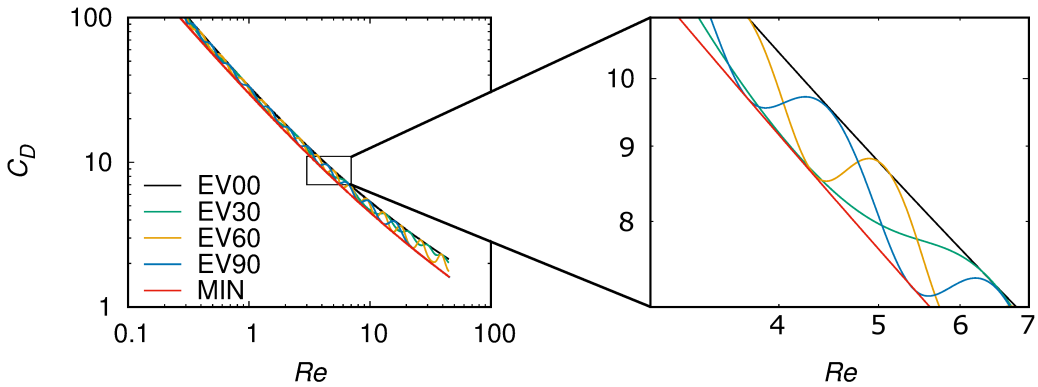

Figure 2.3: Drag curves for EV00, EV30, EV60 and EV90. “MIN” is obtained by the motion of non-rotation(fixed) EV90 particle.

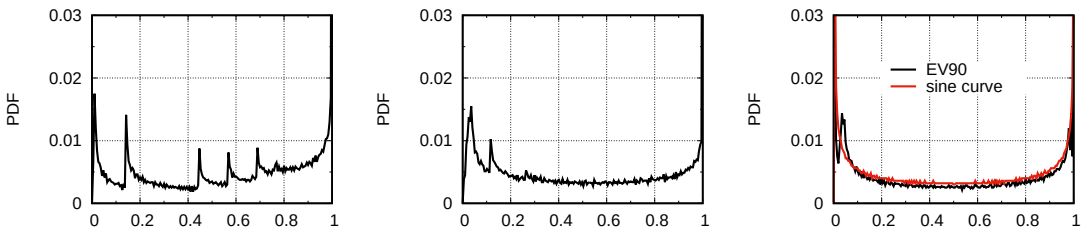

(a) EV30 (b) EV60 (c) EV90 and a sine curve

Figure 2.4: PDF of C_D for (a) EV30, (b) EV60 and (c) EV90, including the PDF of a sine curve. The values on the horizontal axis are normalized by the maximum and minimum C_D values for each case. 0 represents the minimum and 1 represents the maximum.

becomes smaller, and the particle changes its motion mode from oscillation to rotation. In addition, between each spike and the maximum value of C_D at 1.0 on the horizontal axis, the shape of the PDF curve shows a similar behavior with EV90’s but with accumulation. Moreover, the shape of the PDF for EV90 is similar to the sine function’s PDF, suggesting that the PDF of C_D can be expressed by the sine function.

2.3 Spheroidal particle motion model

The results shown in above section imply that the oscillating C_D of the spheroid can be expressed by the PDF of the sine function between the maximum and the minimum C_D

values. Thus, a spheroidal particle's motion can be represented as

$$\log_{10} C_D = \log_{10} C_{Dmin} + (\log_{10} C_{Dmax} - \log_{10} C_{Dmin}) * \frac{sin(2\pi\theta)+1}{2}, \tag{2.7}$$

where θ is a random number between 0 and 1. C_{Dmax} and C_{Dmin} are the C_D values obtained from the spheroidal particle's maximum and minimum C_D curves respectively. These curves are based on the previous section's results using the formula which have a form of the Equation (2.4) proposed by Clift *et al*. [5].

$$C_D = \begin{cases} \frac{24}{Re}(1 + A * Re^{B - C * \log_{10} Re}), & 0.01 < Re \leq 10 \\ \frac{24}{Re}(1 + X * Re^{Y}), & 10 < Re \leq 100 \end{cases} \tag{2.8}$$

where A, B, C, X, and Y are the parameters that are determined by the six degrees of freedom for a particle's motion.

In this model, the random number θ represents the rotation angle of the spheroidal particle. While θ equals 0.75, the C_D reaches C_{Dmin}, means the particle's major axis is parallel to the flow direction, the projection area is smallest thus C_D value also becomes smallest. While θ is 0.25, the C_D becomes C_{Dmax}, means the particle's major axis is perpendicular to the flow direction, the projection area of the particle is largest thus C_D value also becomes largest. The parameters A, B, C, X, and Y must be determined in advance for both the C_{Dmin} and C_{Dmax}.

CHAPTER 3

Particle's shape effect on particle dispersion in an isotropic turbulence flow

3.1 Introduction

Industrial applications around the world utilize gas-particle two-phase flows. For instance, in coal-fired power plants, which are one of the largest industries in terms of power production and CO_2 emission, there is an urgent need to realize clean coal technology to reduce the CO_2 emission. It is important to achieve a much deeper understanding about the two-phase reacting fields on pulverized coal combustion boilers or coal gasifiers, which consume a great amount of coal. However, pulverized coal combustion is a complex phenomenon. The underlying physics governing the simultaneous and interactive dispersion, evaporation, and devolatilization of pulverized coal particles, as well as the heterogeneous and homogeneous reactions are not well understood. For such a flow, Computational Fluid Dynamics (CFD) is frequently used to simulate the flow field. Watanabe and colleagues [9–13] have performed numerical simulations of pulverized coal combustion and gasification on a wide range of reactor scales and investigated the detailed behavior of coal flames.

Many findings in the coal combustion field assumes that coal particles are spherical,

simplifying the numerical problems and reducing the computational cost, but particles prepared by a pulverizer have non-spherical shapes. This assumption, which neglects the real shape of coal particles, is not well assessed and a detailed discussion about the simplification in the literature is limited. Feng, et, al. [14] investigated the fluid force and the torque acting on spheroid settling in fluids, and indicated that the pressure at the stagnation point determines particle's rotation. Broday, et, al. [15] studied the motion of a spheroidal particle moving in a vertical shear flow, and found that a combined effect of the particle's inertia, the flow velocity gradient, and the gravity produces a complicated moving behavior. Mortensen, et,al. [16] studied the orientation of ellipsoidal particles in a turbulent shear flow, and indicated that both the aspect ratio and the equivalent response time are important parameters for the orientation behavior of the prolate particle. The above works are slowly beginning to unravel the motion characteristics of a spheroidal particle, but they only focused on the behavior of a single spheroidal particle. A numerical study to model the effects of a non-spherical particle's shape on the particle's motion and apply the model to industrial problems has not been tried yet. Furthermore, the effects of a non-spherical particle's shape on the dispersion of a large amount of non-spherical particles in a turbulent flow have yet to be investigated. Haider & Levenspiel [6] proposed the drag curve characterized by sphericity of a particle. This can be practically used, namely in the Euler-Lagrangian method, but the effects of rotation and oscillation of a particle are ignored.

It is, therefore, important to model the effects of the non-spherical shape and clarify the impact on the particles' dispersion characteristics in a turbulent flow. In chapter two, the spheroidal particle motion model is developed based on the single spheroidal particle's motion. In this chapter, this motion model is introduced into a computation of a gas-particle two-phase isotropic turbulent flow to investigate the dispersion characteristics of non-spherical particles in a turbulent flow. The results are compared to the behavior of particles with spherical motion model.

3.2 Governing equations

The governing equations of the isotropic turbulent fluid field are the continuous equation and incompressible Navier-Stokes equation, expressed as

$$\frac{\partial \rho}{\partial t} + \frac{\partial \rho u_j}{\partial x_j} = 0, \tag{3.1a}$$

$$\frac{\partial \rho u_i}{\partial t} + \frac{\partial \rho u_j u_i}{\partial x_j} = -\frac{\partial p}{\partial x_i} + \frac{\partial \sigma_{ij}}{\partial x_j} + S_{u_i}, \tag{3.1b}$$

where, ρ, u_i, and p are the fluid density, velocity, and pressure, respectively.

The motion of individual particles moving in the fluid is tracked by Lagrangian method. The governing equations are given by

$$\frac{dx_{i,p}}{dt} = u_{i,p}, \tag{3.2a}$$

$$\frac{du_{i,p}}{dt} = \frac{f_D}{\tau_p}(u_i - u_{i,p}), \tag{3.2b}$$

$$\tau_p = \frac{d_p^2 \rho_p}{18\mu}, \tag{3.2c}$$

where $x_{i,p}$, $u_{i,p}$ and τ_p are the particle position, velocity, and response time, respectively.

S_{u_i} in Equation (3.1b) is the phase coupling term, which is calculated as

$$S_{u_i} = -\frac{1}{\Delta V}\sum_N \frac{m_p f_D}{\tau_p}(u_i - u_{p,i}), \tag{3.3}$$

where m_p is the particle mass. ΔV is the fluid side control volume and f_D is the drag force on particle. f_D in Equations (3.2b) and (3.3) is calculated from the particle's $C_D - Re$ equations.

3.3 Statistical method for the evaluation of the particles' dispersion

In order to quantify the particles' dispersion, the D number [17] and RDF (Radial Distribution Function) are employed to evaluate the characteristics of the particles' dispersion.

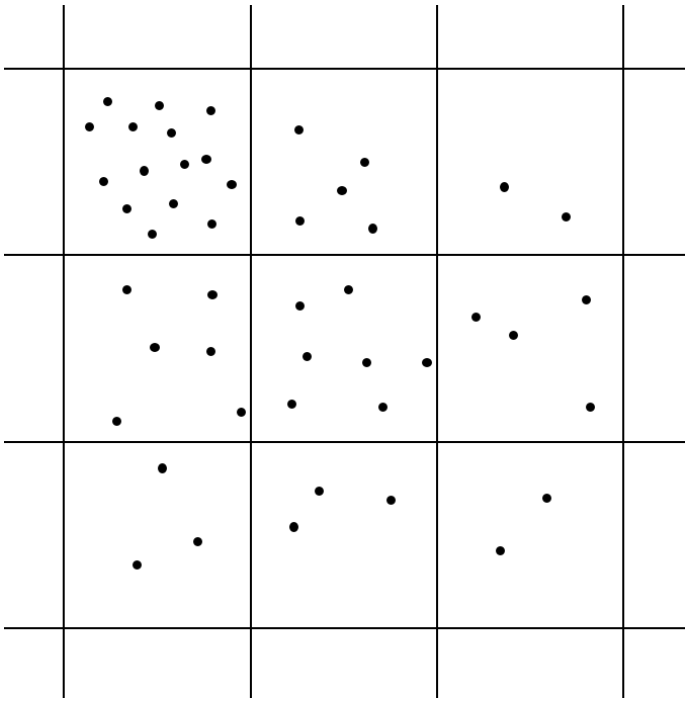

Figure 3.1: The schematic view of the D number method.

The D number identifies the bulk particle clustering and the RDF is used to obtain the detailed distribution behavior around the particles.

3.3.1 D number method

D number method is introduced by Fessler, el, al [17] in their research to investigate the particles distribution in a turbulent channel flow. Note that in Fessler's report, the D number is used in 2D analysis, but it is extended to 3D analysis in this study. Figure 3.1 shows the schematic view of the analysis of the D number. The computational domain is divided into the small box regions to count the number of particles in each box and to estimate the standard deviation, which is compared with that of a random distribution that is defined by the Poisson distribution as

$$F(k) = \frac{e^{-\lambda}\lambda^k}{k!}, \tag{3.4}$$

where λ is the mean number of particles in each box. $F(k)$ represents the probability that k number of particles will be found in a given box. Thus, the D number is defined as

below.

$$D = \frac{\sigma - \sigma_{Poisson}}{\lambda}, \tag{3.5}$$

where σ and $\sigma_{Poisson}$ are the standard deviations.The D number shows the deviation of the targeted particles dispersion from the Poisson distribution. If the particles are extremely unevenly dispersed in space, in some boxes large particle numbers are found, then the standard deviation σ becomes larger, causing an increased D number. For example, in Figure 3.1, the particles are unevenly dispersed. The box on the upper left corner contains more particles than other boxes, thus the σ becomes large, results in a large D number. The D number shows a large positive value when the particles are clustered, which means the particles dispersion differs from the Poisson distribution. But has a positive value close to zero when particles are randomly distributed, indicates the particles dispersion is close to the Poisson distribution. From the definition of the D number, it can be easily understood that the box size affects the results. In this chapter, the box size is determined based on the sensitivity analysis with the various box sizes.

3.3.2 RDF method

Not like D number method, by using the RDF method we can extract the detailed distribution behavior of the particles in terms of the distances between the particles. RDF is defined as

$$g(r_i) = \frac{N_p(i)/\Delta V_i}{N_p/V}, \tag{3.6}$$

where $N_p = N(N-1)/2$ is the total number of particle pairs and V is the volume of the domain. $N_p(i)$ is the total number of particle pairs with a distance between $r_i + \Delta r/2$ and $r_i - \Delta r/2$. ΔV_i is the volume of the shell located at a distance r_i with a thickness Δr. $\Delta V_i = 4\pi[(r_i + \Delta r/2)^3 - (r_i - \Delta r/2)^3]/3$. RDF is the ratio between the particle pair number density at a local shell and the mean value at the whole domain. In other words, RDF describes the characteristics of particle clustering in terms of its length scale. It shows the

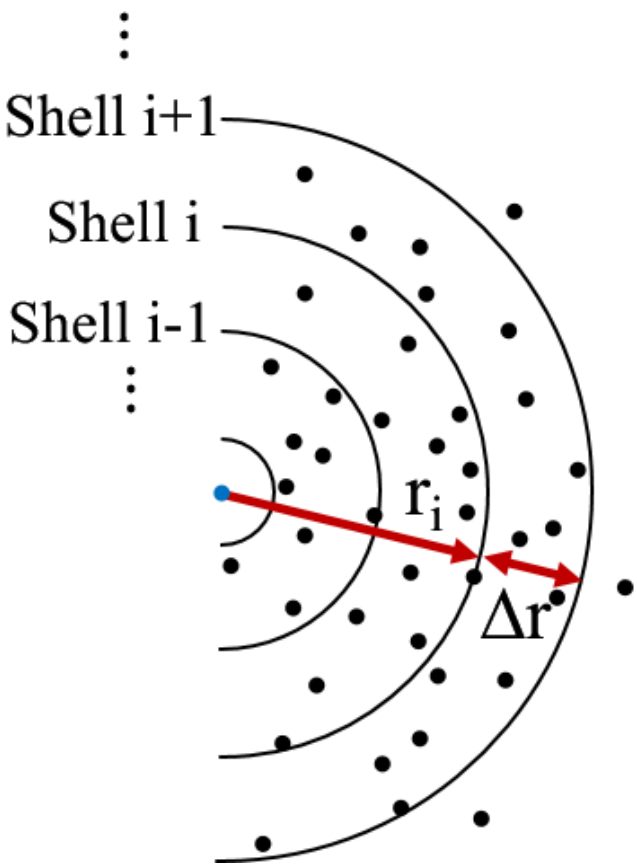

Figure 3.2: The schematic view of the RDF calculation.

frequency of a given distance between two particles appears. For a large RDF value at a distance r_i, it indicates the particle pairs have distance r_i are more than other distance. Thus the particle concentration at this distance is higher, which means the particles are more clustered at this length scale. Figure 3.2 shown the schematic view of the calculation of the RDF value.

3.4 Computational details

In this chapter, totally six cases were performed. Their properties were listed in table 3.1. The spherical case, SV, used the spherical motion model. Other five spheroidal cases used the new spheroidal motion model. The EL96, EL90, and EL85 had the same equivalent radius, which meant the same volume as the SV, but decreasing sphericities. The ES90

Table 3.1: Particle properties used in the $C_D - Re$ equations.

Cases	sphericity[-]	equivalent radius*[m]	major axis a [m]	minor axis $b = c$ [m]
SV	1.00	2.11e−5	2.11e−5	-
EL96	0.96	2.11e−5	3.00e−5	1.78e−5
EL90	0.90	2.11e−5	3.71e−5	1.60e−5
ES90	0.90	1.71e−5	3.00e−5	1.30e−5
EL85	0.85	2.11e−5	4.35e−5	1.48e−5
ES85	0.85	1.46e−5	3.00e−5	1.01e−5

* Equivalent radius is the radius of the sphere which have a equivalent volume.

and ES85 had the same sphericities as the EL90 and EL85, respectively. But their sizes were smaller. The results of these five spheroidal cases were compared with the result of the SV and also compared with each other, to discuss the influence on the particles dispersion of the motion model. For all these six cases, their parameters A, B, C, X, and Y used in the motion model were listed in table 3.2. These parameters were obtained from the single particle calculation.

The computational domain was a $2\pi * 2\pi * 2\pi$ cm^3 cube divided by $128 * 128 * 128$ grids. To maintain the isotropic turbulence, the forcing method by Chen, et, al. [18] was used in this work. To generate the initial condition for the computation, a single-phase isotropic turbulent flow was generated and developed in 1000 steps. Then 9000 steps were calculated and the particles' Stokes number Stk, the values of the D number and RDF were averaged. The time step was updated in each step by the constant CFL, which was set to 0.5. The particles were tracked by the Lagrangian manner with the PSI-CELL method. In order to organize the results in terms of the Stokes number Stk for each case, the diameters of the particles were adjusted. For example, for the case SV, the diameter of the particles varied from 5 μm to 66.44 μm, resulted in a Stk range from 0.03 to 5. For the result analysis, $24 * 24 * 24$ boxes were used to evaluate the D number.

Figure 3.3 shows the distribution of the vortices distinguished by the second invariant

Table 3.2: Parameters A, B, C, X, Y used in each case.

Cases	curve	A	B	C	X	Y
SV	C_D	-	-	-	0.311	0.528
EL96	C_{Dmax}	0.387	0.321	0.206	0.307	0.600
	C_{Dmin}	0.258	0.400	0.138	0.245	0.556
EL90	C_{Dmax}	0.525	0.299	0.171	0.389	0.583
	C_{Dmin}	0.264	0.407	0.087	0.236	0.542
ES90	C_{Dmax}	0.506	0.320	0.203	0.389	0.583
	C_{Dmin}	0.250	0.376	0.171	0.232	0.544
EL85	C_{Dmax}	0.697	0.268	0.175	0.497	0.563
	C_{Dmin}	0.307	0.348	0.091	0.255	0.514
ES85	C_{Dmax}	0.694	0.368	0.223	0.592	0.500
	C_{Dmin}	0.296	0.382	0.227	0.259	0.511

of the velocity-gradient tensor, $Q_2 = 10000$, after the turbulent is fully developed. Q_2 is the second invariant of the velocity gradient tensor, indicating that the vortex region has a positive value [19]. Long stretched vortices are formed and the isotropic turbulent flow field is generated correctly.

3.5 Results and discussion

Figure 3.4(a) shows the scatter plots of C_D against Re for ES85 at $Stk \approx 2.2$ for all steps. Most Re numbers are between 0.1 and 1. Figure 3.4(b) shows the PDF of C_D. The PDF of C_D overlaps with the sine function's PDF, confirming that Equation (2.7) precisely captures the behavior of a spheroidal particle.

Figure 3.5 shows the variations in the D number and the Stk number in the calculation of ES85 at $stk \approx 2.5$. The time-averaged values of the D number and the Stk number reach the steady state after certain step, while the instantaneous values vary. Consequently, the

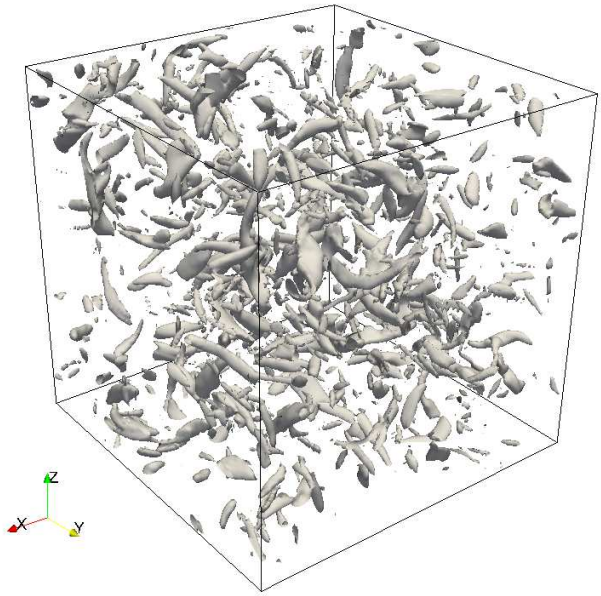

Figure 3.3: Visualization of the vortex defined by $Q_2 = 10000$ for SV.

time-averaged value at the last step represents the particles' distribution behavior in this work.

3.5.1 Results of D number method

Figure 3.6 compares the relationship between the D number and the Stk number for the six cases. In the lower Stk number region where the left side of the peak value of the D number appears, SV has the largest D number followed by EL96, EL90, and ES90. EL85 and ES85 have the smallest D numbers. However, in the higher Stk number region where the right side of the peak value of the D number appears, the order is reversed: EL85 and ES85 have the largest D numbers while SV has the smallest one. Particles with the same sphericity but different sizes have almost the same D number because similar shapes, which are determined by the same sphericity, have the same $C_D - Re$ relation. Another property is that all these particles have almost the same peak value but the peak position varies slightly according to the shape.

Comparing the curves of different particle sphericities (SV, EL90 and EL85 in Figure

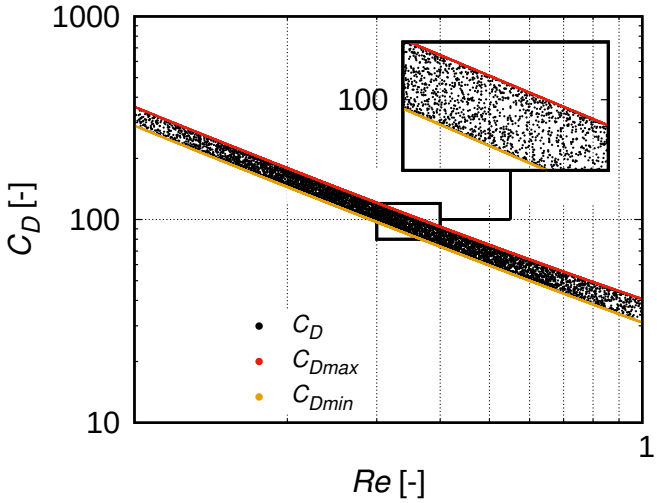

(a) C_D and Re variation during a simulation of a particle for ES85 with $stk \approx 2.2$.

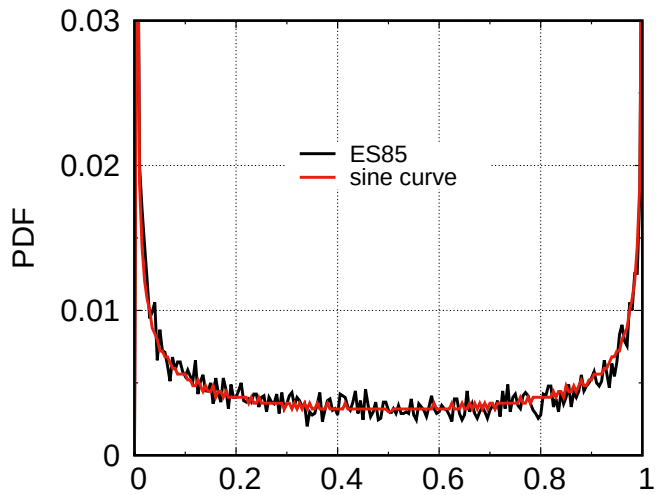

(b) PDF of the particle's C_D value.

Figure 3.4: Drag coefficient of a spheroid and its PDF curve.

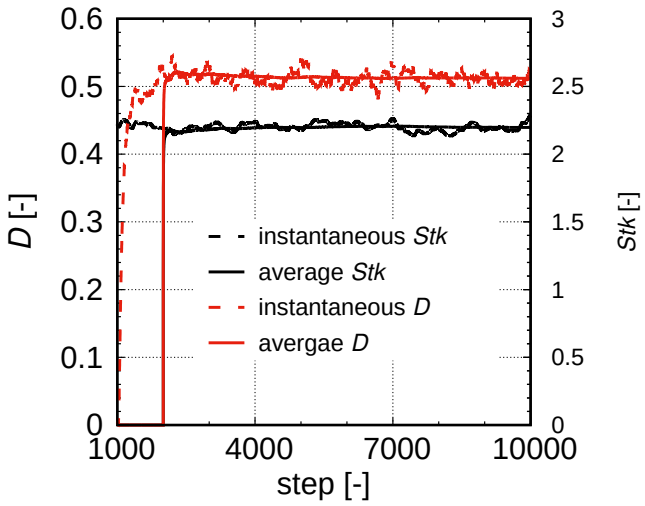

Figure 3.5: Variations in the D number and the Stk number in the calculation of ES85.

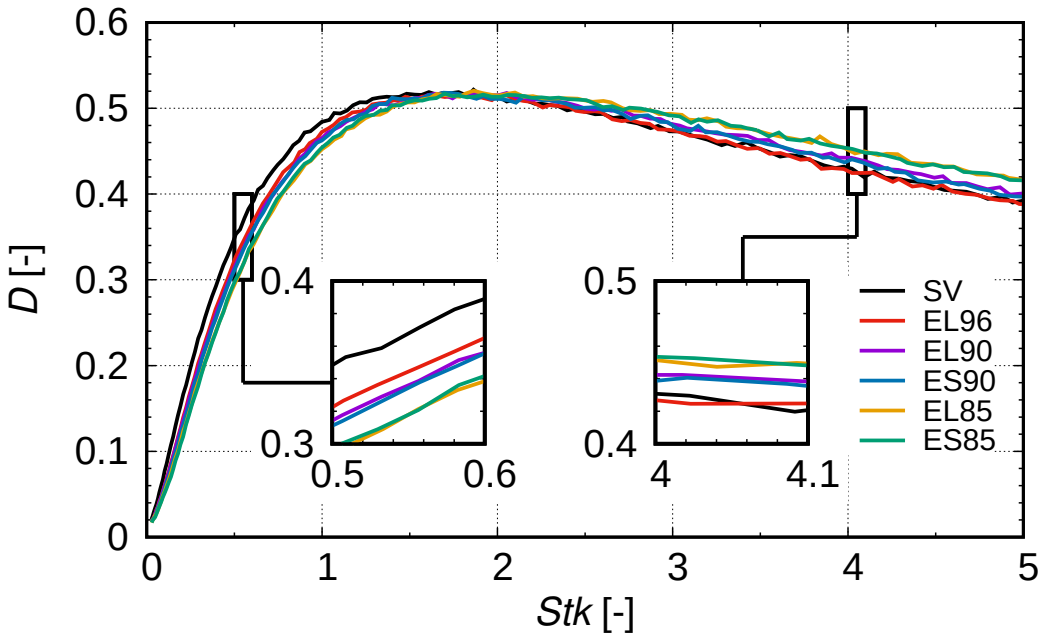

Figure 3.6: Comparison of the D number by case.

3.6), as the sphericity increases, the *D*-*Stk* curve shifts toward the right hand side, changing the order of the *D* number between the lower and the higher *Stk* number regions where the peak value of the *D* number appears.

Figure 3.7(a) shows the corresponding $C_D - Re$ relations. EL90 and EL85 have the same C_{Dmin} but different C_{Dmax}, EL85 has a larger C_{Dmax}. SV's C_D curve is located between the maximum and minimum C_D values of spheroidal particles but approaches the minimum one as the *Re* number becomes smaller. The mean C_D curve of the spheroids, which represents the particle's moving behavior, can be decomposed into a right horizontal shift and an upward vertical shift of sphere's C_D curve. The right horizontal shift keeps C_D constant but enlarges *Re*. Conversely, the upward vertical shift keeps *Re* constant but enlarges the C_D value. However, from the definition of C_D and *Re*, Equation (2.3), it can also be written as,

$$C_D = \frac{8\rho_f F_D}{\pi\mu^2 Re^2}, \tag{3.7}$$

It can be shown that $C_D \propto 1/Re^2$. Hence, a small variation in *Re* causes a large change of C_D, but a large change of C_D has a negligible effect on *Re*. Thus, the right horizontal shift has a greater impact on the particle's behavior. For the spheroid, this means the diameter d'_p, which can represent the particle's motion is larger than that for a sphere's. Namely, the spheroid's τ'_p is larger than that of the sphere's, causing a larger Stk'. As the sphericity becomes smaller, this effect becomes larger, which is why the spheroid's *D* number curve shifts to the right as the sphericity decreases.

Next compare the curves of the sphere and the spheroid with a sphericity of 0.96 (SV and EL96 in Figure 3.6). On the left side of the peak, the *D* numbers for the sphere and spheroid differ, but are almost identical on the right side of the peak. This indicates that in the small *Stk* number region, the particles' dispersion is more sensitive to the sphericity than the large *Stk* number region. Figure 3.7(b) shows that in small *Re* number region, which corresponds to the small *Stk* number region, the C_D curve of SV is close to the C_{Dmin} of EL96, the rightwards shift of the *D* number appears in the small *Stk* number region. However, in the relatively large *Re* number region, the sphere's C_D curve is located in the

middle of EL96's C_{Dmax} and C_{Dmin}, causing overlap between these two D number curves.

3.5.2 Results of RDF method

Figure 3.8 shows the characteristics of RDF for the cases of $Stk = 0.5, 1.0, 1.9$, and 4.6. r/η is the ratio between the distance from a particle and Kolmogorov length scale, where a large r/η means far away from a particle. In this work, η is about 0.02147cm for all cases. The small boxes used in the D number analysis are about 0.2618cm or 12 times η. Therefore, on the right side of $r/\eta = 12$, the results of RDF reflect the D number analysis results. The results of RDF when $r/\eta < 12$ show detailed distance information of the particles' dispersion, which cannot be obtained from the trend of the D number. For $Stk = 0.5$, a well-marked difference is observed in each case. As the sphericity becomes smaller, the RDF values also becomes smaller, indicating the number of particles at a very close distance from a given particle is less, the particles tend to be randomly distributed. For $Stk = 1.0$, all the results almost overlap, showing that they have the same particle number density around a certain particle. Additionally, all the results become larger than the results of $Stk = 0.5$, meaning the particles are more clustered at $Stk = 1.0$. As the Stk number becomes larger, the RDF values in all cases become smaller again. Unlike the small Stk numbers, with an decreased sphericity, the RDF values become larger, indicating the particles are more clustered. These results agree well with the D number analysis results.

Nevertheless, a difference can be found between the D number analysis and the RDF method. For the D number analysis, peak particles clustering appears around $Stk = 1.5$ to $Stk = 2.0$, whereas the particles show peak clustering around $Stk = 1.0$ for the RDF method. As mentioned above, the small boxes used in the D number analysis are about 12 times η. Figure 3.9, which shows the sum of the $g(r)$ values when $r/\eta < 12$, demonstrates how particles cluster at this scale. In all cases, as the Stk number increases, the $g(r)$ value initially increases but then decreases again, agreeing with the result of the D number analysis. Around $Stk = 1.0$, all cases except SV show the peak value, indicating that the particles are most clustered at this Stk number.

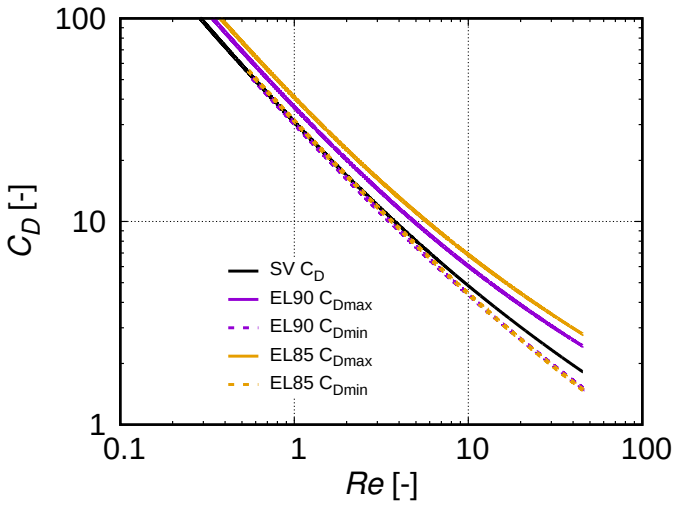

(a)

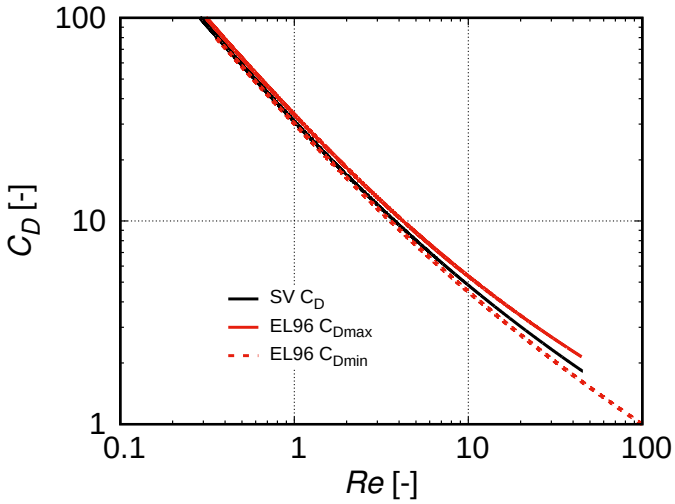

(b)

Figure 3.7: (a) Comparison of the C_D curves between SV, EL90 and EL85. (b) Comparison of the C_D curves between SV andEL96.

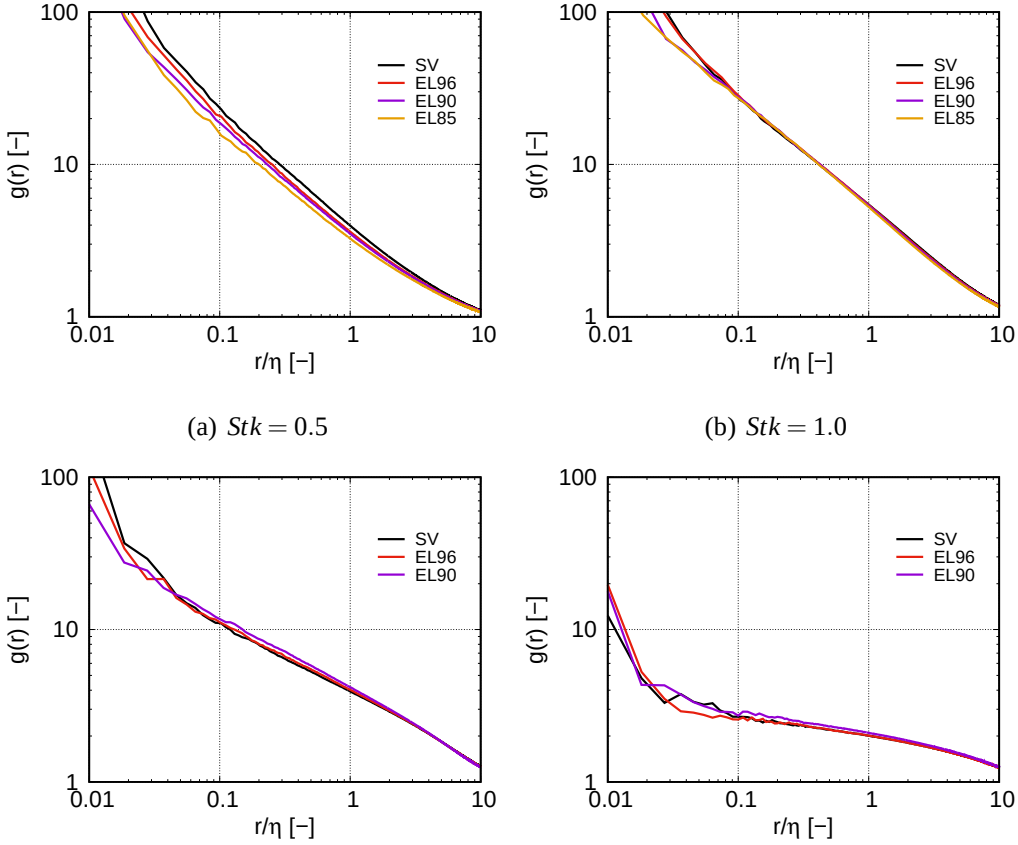

(a) $Stk = 0.5$ (b) $Stk = 1.0$

(c) $Stk = 1.9$ (d) $Stk = 4.6$

Figure 3.8: RDF results at four certain Stk numbers.

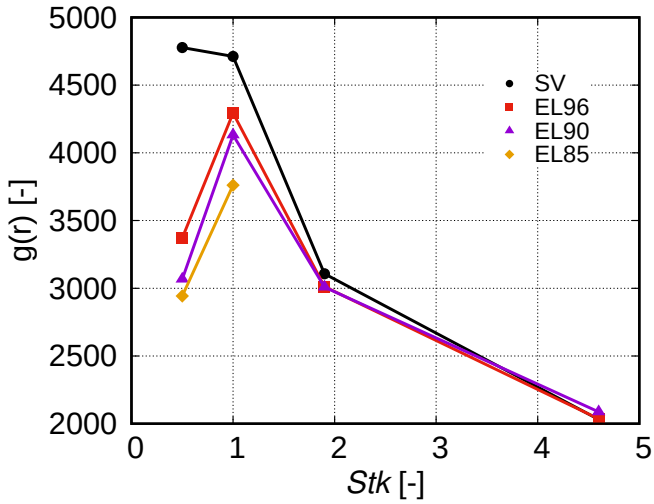

Figure 3.9: Sum of $g(r)$ values while $r/\eta < 12$ for each case.

3.6 Chapter conclusion

In this chapter, the numerical simulation on particles dispersed in an isotropic turbulent flow, are performed to investigate the effects of a particle's shape on a particle's motion by employing spherical and spheroidal particle motion model.

The simulation demonstrates that the particles' shape affects the dispersion behavior. Between $Stk = 1$ to 2, both the spherical and the spheroidal particles have the same peak value of the D number, but in the small Stk region, particles with a larger sphericity tend to be more clustered. In contrast, in the large Stk region, particles with a larger sphericity tend to be randomly distributed. Additionally, particles with the same sphericity exhibit similar dispersion behavior regardless of the particle's size, implying that the sphericity can characterize the dispersion properties. In the large Stk region, spheroidal particles have an extremely large sphericity, which is close to unity, their dispersions are similar to those of spherical particles. However in the small Stk region, the dispersion characteristics of spheroidal particles significantly differ from those of spherical particles. Spheroidal particles' dispersion is much more sensitive at a low Stk number than at a large Stk number. Consequently, in the large Stk number region, a particle with a large sphericity can be treated as a spherical particle.

CHAPTER 4

Particle's shape effect on particle dispersion in a jet flow

4.1 Introduction

As the previous chapter mentioned, many findings in the coal combustion field assume that coal particles are spherical to simplify the numerical problems and reducing the computational cost. However, neglecting the particle's shape results in a decrease in the accuracy of the simulation. Due to the lack of relevant experimental researches, how much the accuracy reduced is not revealed. In chapter two, a spheroidal motion model is proposed. In chapter three, this model is validated in an isotropic turbulent flow field with mono-diameter particles. It shows the particles' dispersion has been affected by the particle's motion model. Therefore we can consider that by using different particle motion model, the results of the simulation in a coal combustion or gasification field will differ.

In this chapter, firstly an experiment is done to investigate the difference of the particle dispersion of the pulverized coal and spherical polymer particles in a jet burner. Then a simulation which applies the experimental condition is performed using the particle's spheroidal and spherical motion model. The Large-eddy simulation (LES) method is used to reduce calculation cost. The simulation results are compared with the experimental results. The particle's shape effect and diameter distribution effect on the particles dispersion are discussed and summarized.

Table 4.1: The cases performed in the experiment.

	cases	particle shape	diameter [μm]
Exp.	COAL	complex	-
	POLYMER	spherical	28

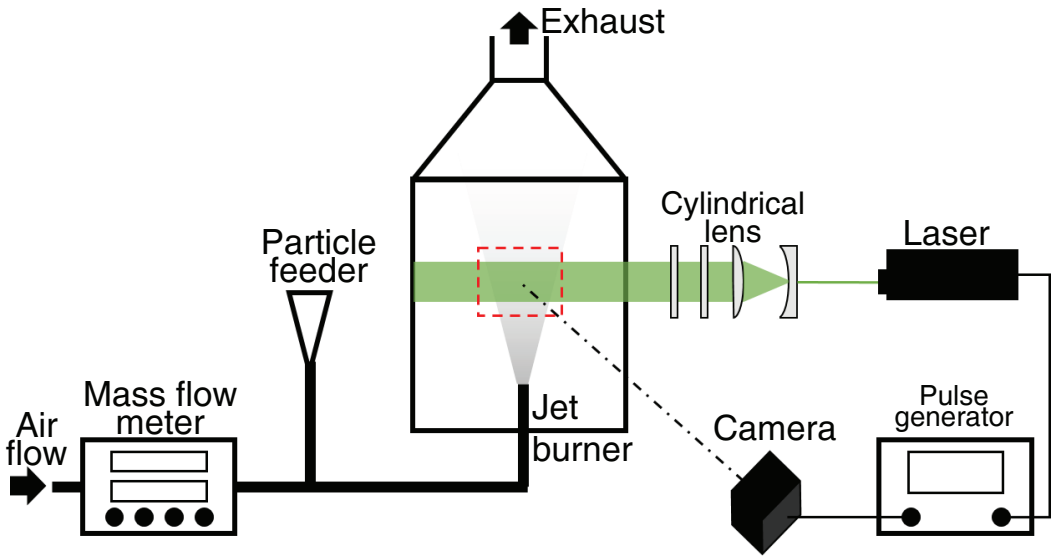

Figure 4.1: The schematic design of the experiment configuration.

4.2 Experimental details

Figure 4.1 shown the schematic diagram of the experiment. In this experiment, the particles were transported by the air flow and injected vertically into space via a jet burner. After the injection, a laser sheet was deployed and the particles behavior was caught by Particle Image Velocimetry (PIV) method. The laser sheet was applied at a different height of 0, 20, 30, 60, 90, 120, 150, 180, and 210 mm from the burner exit. At each height, 1000 graphics of the particles' instantaneous motion were taken. The particles' instantaneous and time-averaged Mie scatting and velocity profiles were obtained from the PIV. Two cases were performed, one used pulverized coal and the other used spherical polymer particles. The details of the particles were listed in table 4.1. The COAL case used pulverized coal, which had a composition of complex shape. The diameter mainly

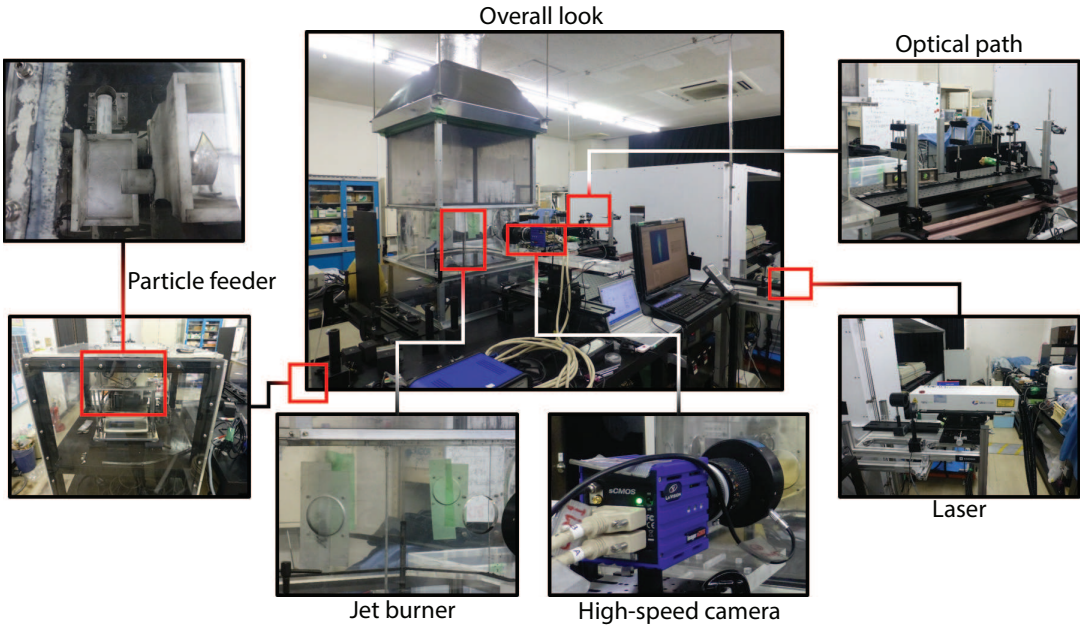

Figure 4.2: A look of the experiment.

distributed in a range from few tens to hundreds micrometer. For the POLYMER case, the particle was made of polymer, which density was about 1200 kg/m^3. The shape was spherical and the diameter was highly concentrated. During the experiment, both the particle mass flux rate and the gas flow rate were measured and adjusted to be constant. In this study, the averaged flow velocity was adjusted to 7.59 m/s and the particle mass flux rate was kept 1.29194e-4 kg/s.

Figure 4.2 shows a look of the experiment.

4.3 Numerical methods

4.3.1 Governing equations

In the simulation, the LES is applied. The governing equations of the gas phase are expressed as

$$\frac{\partial \overline{\rho}_f}{\partial t} + \frac{\partial \overline{\rho}_f \widetilde{u}_j}{\partial x_j} = 0, \tag{4.1}$$

$$\frac{\partial \overline{\rho}_f \widetilde{u}_i}{\partial t} + \frac{\partial \overline{\rho}_f \widetilde{u}_j \widetilde{u}_i}{\partial x_j} = -\frac{\partial \overline{p}}{\partial x_i} + \frac{\partial \overline{\sigma}_{ij}}{\partial x_j} + \frac{\partial \tau_{u_i}}{\partial x_j} + \overline{\rho}_f g + S_{u_i}, \tag{4.2}$$

$$\frac{\partial \overline{\rho}_f \widetilde{h}}{\partial t} + \frac{\partial \overline{\rho}_f \widetilde{u}_j \widetilde{h}}{\partial x_j} = \frac{\partial}{\partial x_j}(\overline{\rho}_f a \frac{\partial \widetilde{h}}{\partial x_j}) + \frac{\partial q_h}{\partial x_j}. \tag{4.3}$$

here ρ_f, u_i, p, h, σ_{ij}, and a are the gas phase density, velocity, pressure, enthalpy, viscous stress tensor, and thermal diffusivity, respectively. $\tau_{u_i u_j}$ and q_h are the subgrid-scale (SGS) effects in LES. $\overline{\ }$ and $\widetilde{\ }$ denote the the spatial and Favre filtering.

For the individual particles moving in the fluid, their motion is tracked by Lagrangian method. The governing equations are given by

$$\frac{dx_{i,p}}{dt} = u_{i,p}, \tag{4.4}$$

$$\frac{du_{i,p}}{dt} = \frac{f_d}{\tau_p}(\widetilde{u}_i - u_{i,p}) + g, \tag{4.5}$$

here $x_{i,p}$, $u_{i,p}$ and τ_p are the particle position, velocity, and response time, respectively. f_d is the correction of the drag force acting on the particle. In this study, the empirical spherical model and the new developed spheroidal model in chapter two are used respectively.

The S_{u_i} in Equation (4.2) is the interactions between the gas and solid particle phases, written as

$$S_{u_i} = -\frac{1}{\Delta V}\Sigma[\frac{m_p f_d}{\tau_p}(\widetilde{u}_i - u_{i,p}) + \frac{dm_p}{dt}u_{i,p}]. \tag{4.6}$$

where ΔV is the control volume of the gas phase.

4.3.2 Evaluation of particle number intensity

The Mie scattering of the experimental results is related to the particle numbers. A high luminance of the Mie scattering means more particles and low luminance means few particles. Thus in this study, for the simulation results, we calculate the particle number intensity in order to compare with the experimental results. The particle number intensity is calculated as

1. A slice of all the particles is taken. The slice emulates the laser sheet and its thickness is set to 1.2 mm.

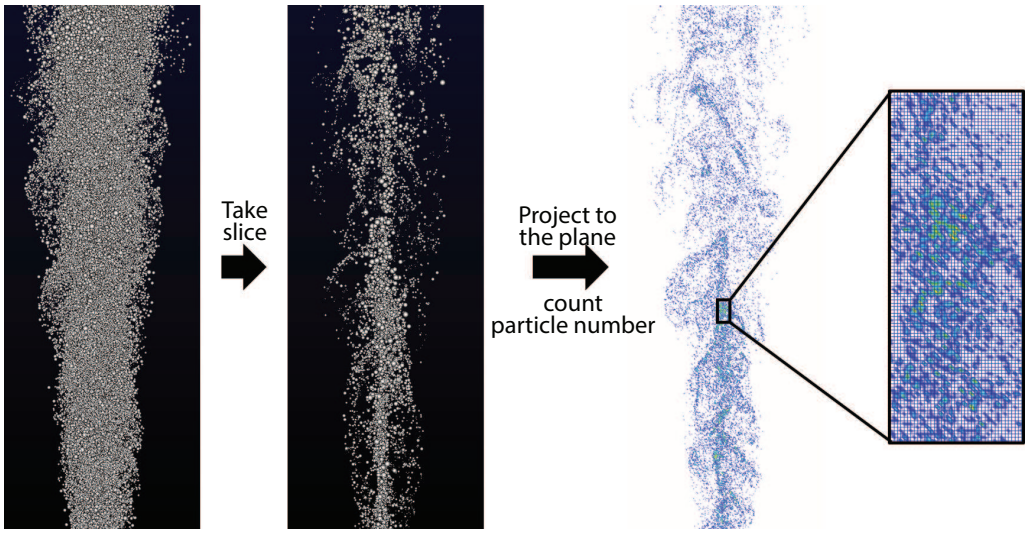

Figure 4.3: The procedure to calculate the particle number intensity.

2. The particles located in the slice are projected to a plane which is divided into small boxes.

3. The particle numbers in each box are counted.

4. The particle number is normalized to a range of [0,255] for post-processing and represent the Mie scattering.

Figure 4.3 shows the procedure of calculation of the particle number intensity.

The particle number intensity is taken averaged to make a time-averaged Mie scattering look-like result, show as Figure 4.4.

4.4 Computational details

In the simulation, totally four cases were performed, shown in table 4.2. These four cases were dived into two groups, the G_SPE group used the spherical motion model, while the G_SPO group used the spheroidal motion model. By comparing these two groups, the particle's shape effect were discussed. Furthermore, in each group, there were one case with mono-diameter and one case with diameters ranging from 5 to 100 μm to discuss the diameter distribution influence. All the particles had the same density of 1200 kg/m^3, the

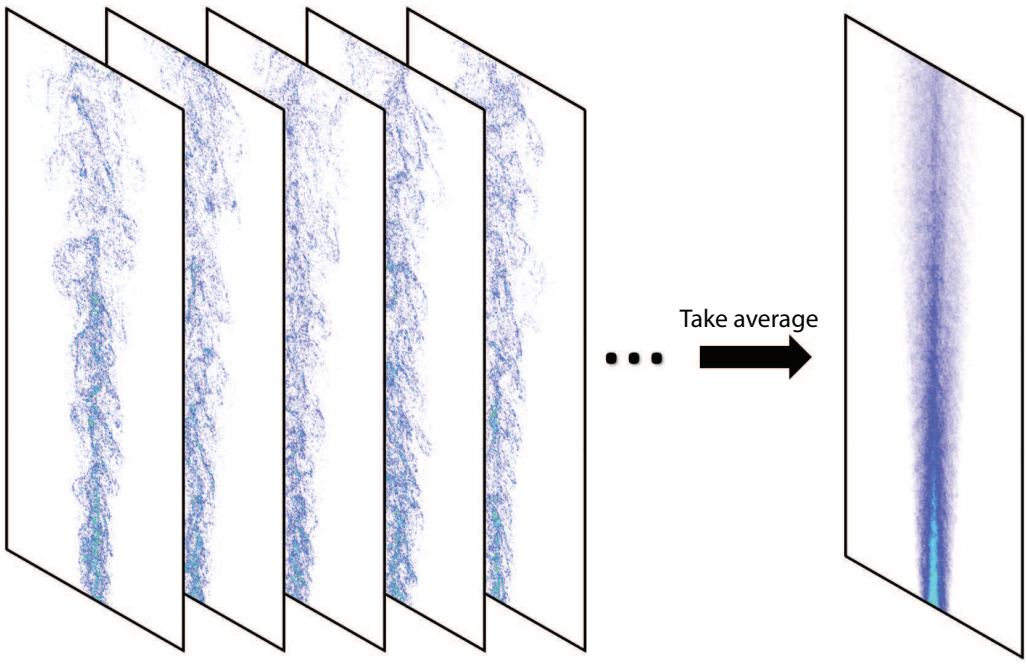

Figure 4.4: By average various instantaneous particle number intensity figures, we finally get a averaged Mie scattering look-like result.

Table 4.2: The cases performed in the simulation.

	group	cases	particle model	diameter [μm]
Sim.	G_SPE	SPE_S	spherical	28
		SPE_R	spherical	5,20,40,60,80,100
	G_SPO	SPO_S	spheroidal	28
		SPO_R	spheroidal	5,20,40,60,80,100

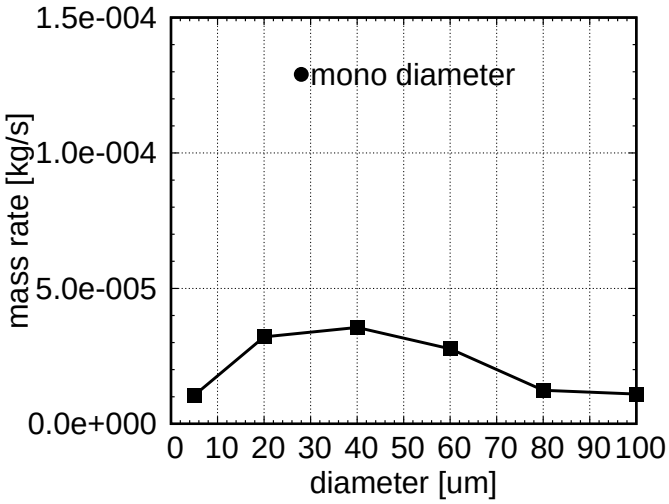

Figure 4.5: The particle mass flux rate of different diameters.

same as the POLYMER. The mass flux of the particles was the same as the experiment's. For the cases with diameter distribution, each diameter had different mass flux rate, were plotted in Figure 4.5. For the cases with the mono-diameter of 28 μm, their mass flux of the particles was the summation of the mass flux of all the diameters in the cases with diameter distribution. The particles were injected into the flow vertically and had an initial velocity of 7.59 m/s.

The computational domain was a 0.36m cylinder with a diameter of 0.1 m. The jet burner located at the bottom of the domain, had a 6 mm diameter and 60 mm height. The exit of the burner was set to be y=0. The gas flow velocity in the burner was set by using a turbulent flow database made by Kempf, et, al. [20]. This database was based on the experimental observations of this jet burner. The domain was shown in Figure 4.6.

4.5 Results and discussion

4.5.1 Velocity profile

Figure 4.7 shows the averaged vertical velocity of the particles at different heights. With the height rising, the vertical velocity decreases. The POLYMER's velocity is always larger than the COAL's velocity. This difference becomes largest at the low-middle height

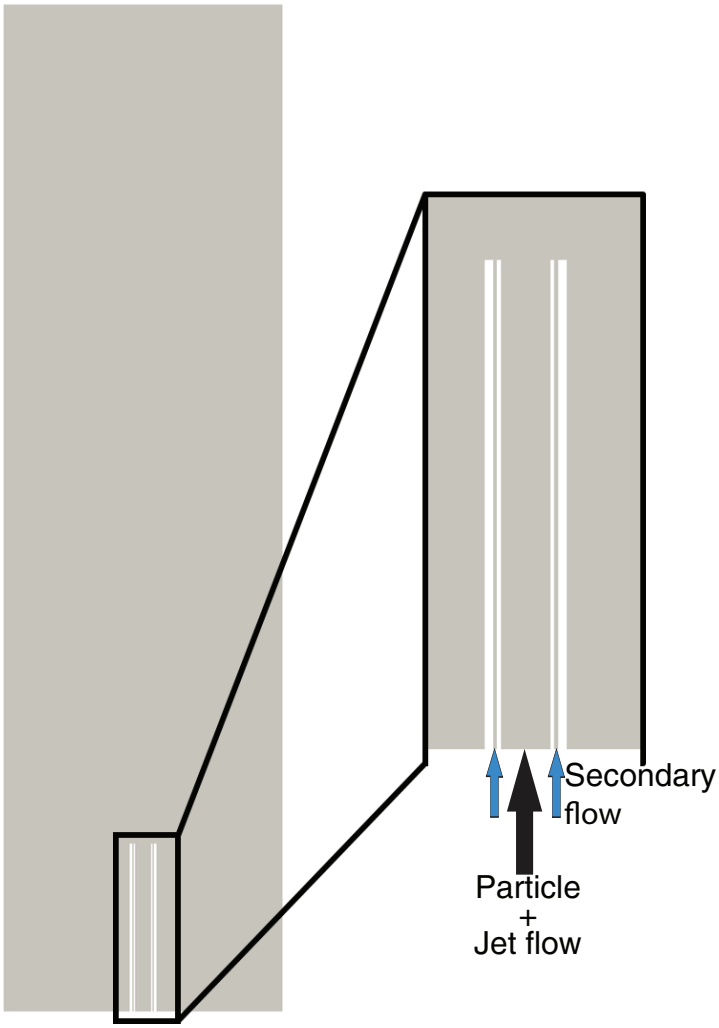

Figure 4.6: Calculation domain of the simulation.

of about 60 mm. Then the difference becomes smaller at higher heights. The simulation results are in good agreement with the experimental results at the lower and middle heights, but larger than the experimental results at the higher height. At lower height near the jet burner, the velocity of the simulation is a little smaller than the velocity of the experiment. However, as the height increases, the velocity of the simulation becomes larger than the experimental results. At y = 210 mm, shown in Figure 4.7(h), the particle velocity of simulation is about 1.5 times compared to the experimental results. Another thing can be noticed is that the difference between the two particle motion models is not obvious. At all heights, there is no difference between the group G_SPE and G_SPO, indicates that the particle vertical velocity is not affected by the motion model significantly. At low-middle height of about 60 and 90 mm, the cases with diameter distribution, SPE_R and SPO_R, have a smaller velocity than that of the cases with mono-diameter, SPE_S and SPO_S. This agrees with the results of the experiment, that the mono-diameter particles' velocity is larger.

Figure 4.8 shows the standard deviation (SD) of the vertical velocity of each case. By using the SD values, the variation of the vertical velocities can be analyzed. The SD values become smaller as the height increases, indicates the particle vertical velocity becomes closely distributed around the mean value. For the experiment cases, the difference between the COAL and POLYMER is not significant. However, for POLYMER at lower heights, there are large disorders. This may be caused by the measurement error. For the simulation cases, the SD values are always smaller than the experimental results. This difference becomes obvious at higher heights. Which means in simulation cases, the particles have highly concentrated velocities thus the SD values becomes small. The difference of the SD values of the four simulation cases are not obvious, indicates the SD values are not affected by the particle motion model or the diameter distribution significantly.

Figure 4.9 shows the averaged radial velocity at different heights. For all the experiment and simulation cases, they show a high similarity. However, only the POLYMER case shows an unusual behavior. At lower heights, the POLYMER shows a violent varia-

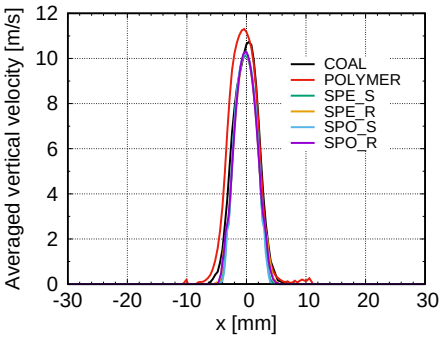

(a) y=20 mm

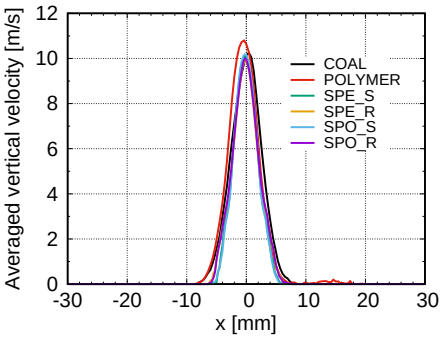

(b) y=30 mm

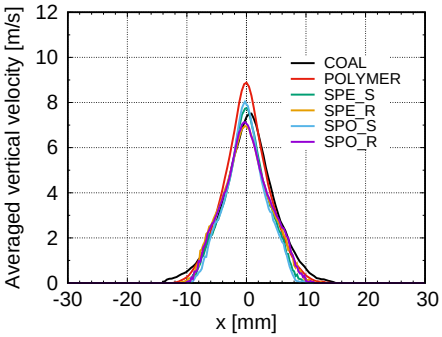

(c) y=60 mm

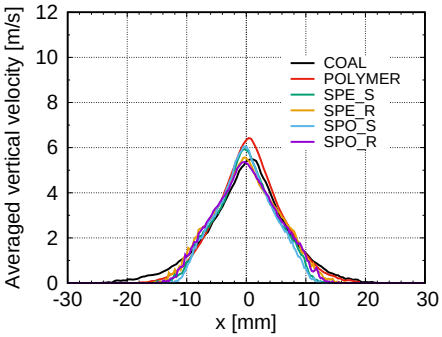

(d) y=90 mm

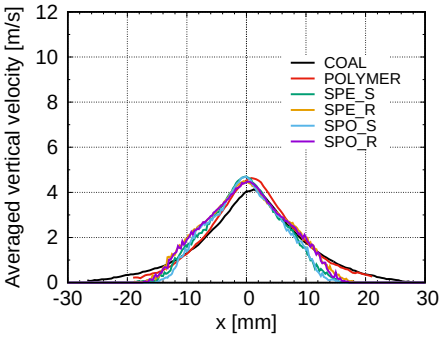

(e) y=120 mm

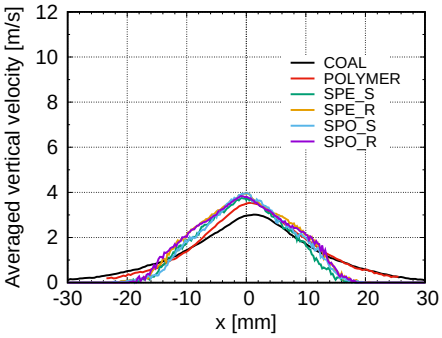

(f) y=150 mm

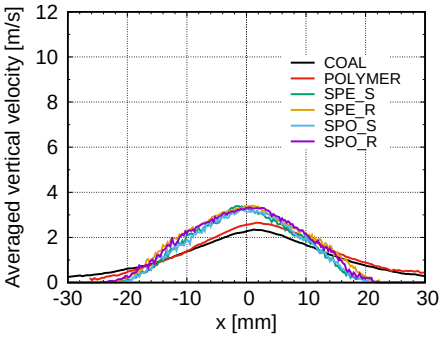

(g) y=180 mm

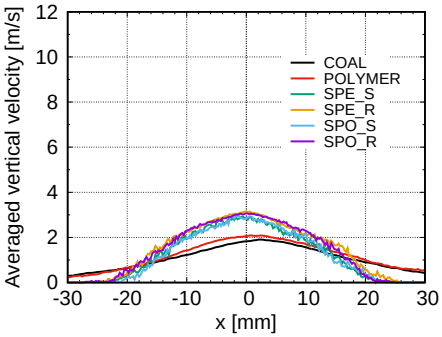

(h) y=210 mm

Figure 4.7: Averaged vertical velocity at different height for all the cases.

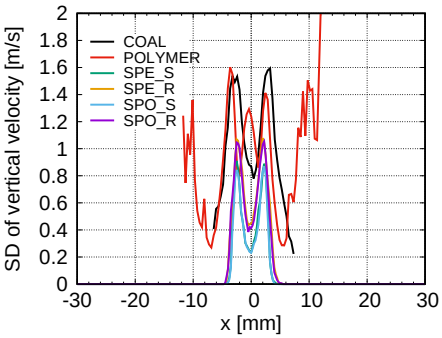

(a) y=20 mm

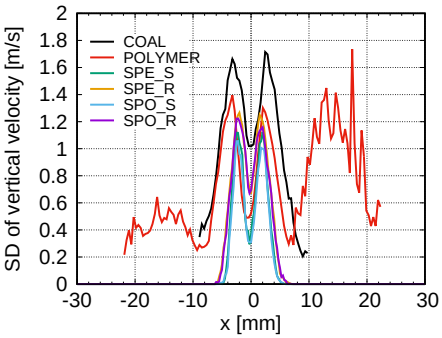

(b) y=30 mm

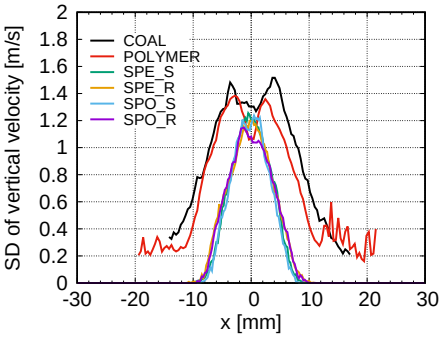

(c) y=60 mm

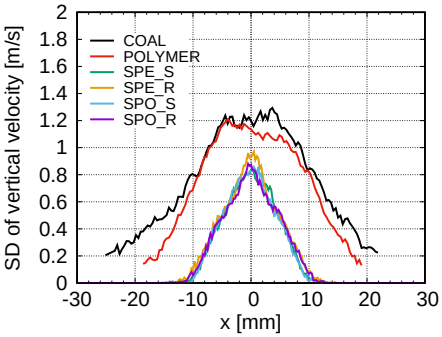

(d) y=90 mm

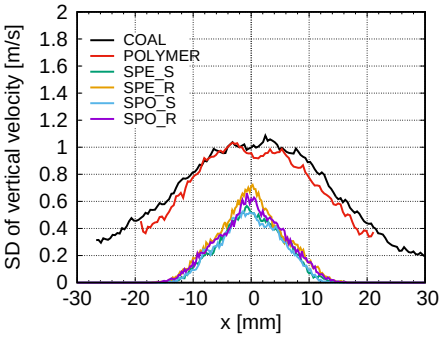

(e) y=120 mm

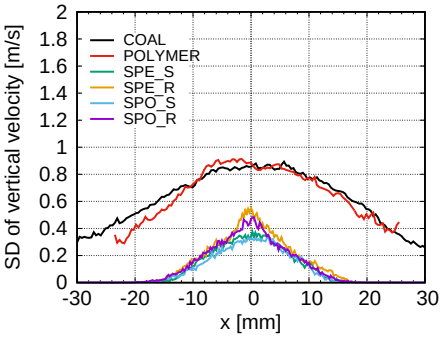

(f) y=150 mm

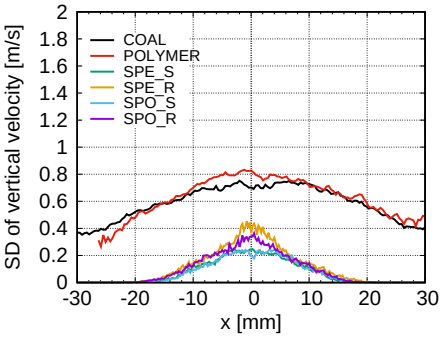

(g) y=180 mm

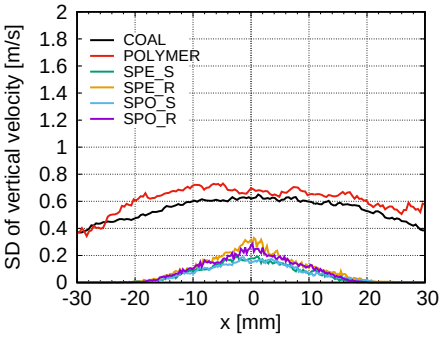

(h) y=210 mm

Figure 4.8: Standard deviation of the vertical velocity at different height for all cases.

tion which is considered as the measurement error. At higher heights, the POLYMER has a much larger radial velocity than the COAL and simulation cases, almost double. Despite this, the COAL and the four simulation cases have the same radial velocity variation.

Figure 4.10 shows the SD values of the radial velocity. The results are similar to the results of the vertical velocity shown in Figure 4.8. If we ignore the disorder part of the POLYMER at lower heights (may be caused by measurement error), we found that at lower heights, the SD values of COAL is larger than the POLYMER's. As the height increasing, the SD values of the COAL and POLYMER first increase and then decrease. The peak appears at y = 60 mm for both the two experiment cases. However, although the peak SD value of the COAL is much larger than the POLYMER's, since it decreases much faster, the COAL's SD values becomes a little smaller than the POLYMER's at higher heights. This indicates that the COAL's radial velocity varies much more intense than the POLYMER's. For the simulation cases, the results are much smaller than the experimental results from the lower to the higher heights. There is no difference between the group G_SPE and G_SPO, but obvious difference between the cases with and without diameter distribution. Similar to the experiment results, the SD values of the simulations first increase then decrease. At higher heights, all the four simulation cases have almost the same SD values.

From the analysis of the vertical and radial velocity profiles above, it shows the simulation cases are in agreement with the experiments. For the two experiment cases, the velocity profiles are not very different. For the four simulation cases, some differences have been observed at the higher heights compared with the experiment. This may due to the resolution of the mesh. In order to reduce the calculation cost, the resolution at higher heights has been reduced. Since the LES method is used, the mesh at higher heights may be coarse thus the eddies may become weaker or disappear. Therefore the influence from the eddies becomes weaker and the particles' motion becomes weaker. Another thing to note is that the difference between the spherical and spheroidal models are not significant. The difference observed in the simulation cases are mainly caused by the diameter distribution effect.

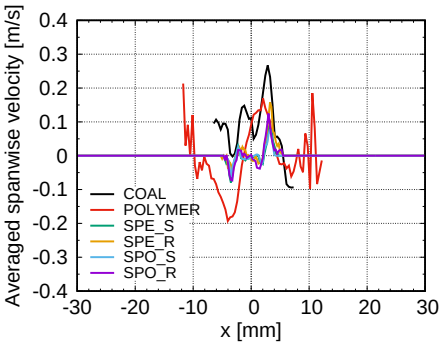

(a) y=20 mm

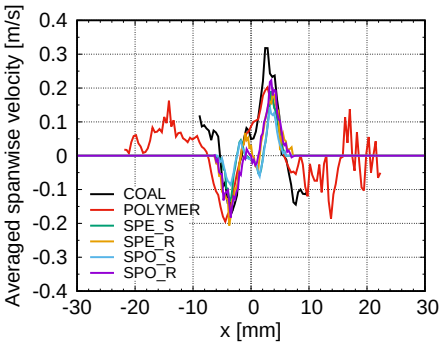

(b) y=30 mm

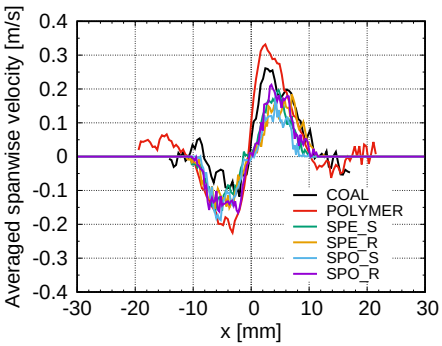

(c) y=60 mm

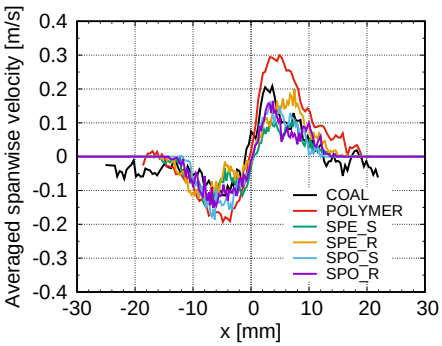

(d) y=90 mm

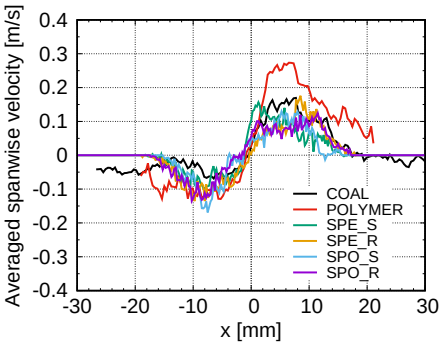

(e) y=120 mm

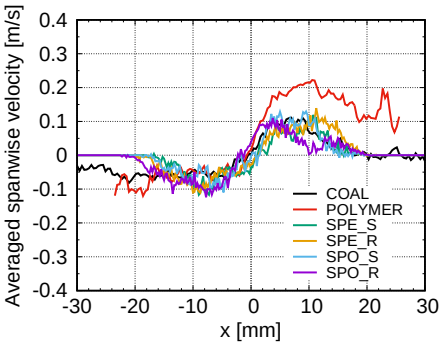

(f) y=150 mm

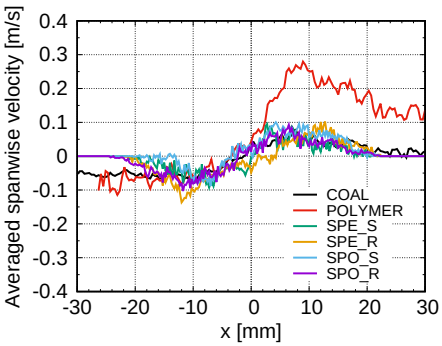

(g) y=180 mm

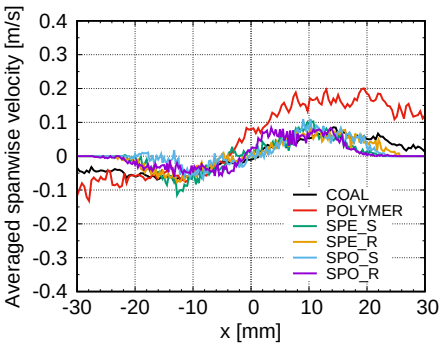

(h) y=210 mm

Figure 4.9: Averaged radial velocity at different height for all the cases.

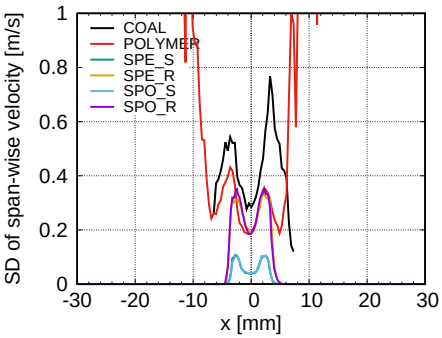

(a) y=20 mm

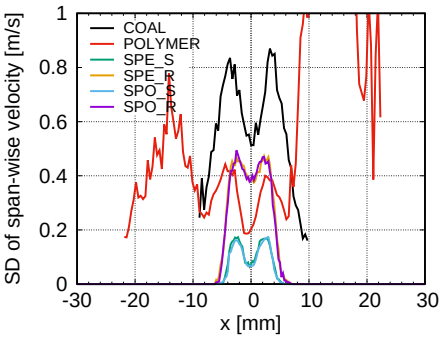

(b) y=30 mm

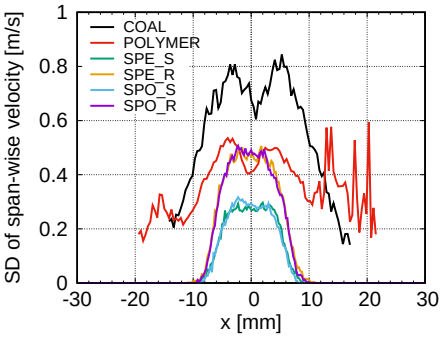

(c) y=60 mm

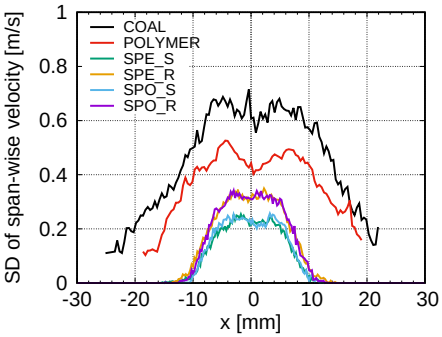

(d) y=90 mm

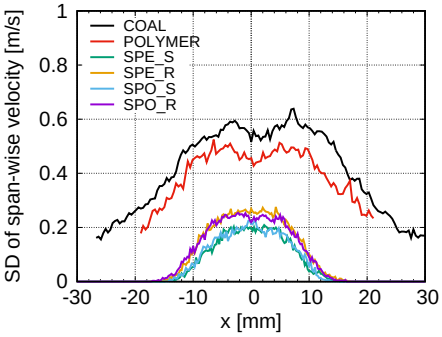

(e) y=120 mm

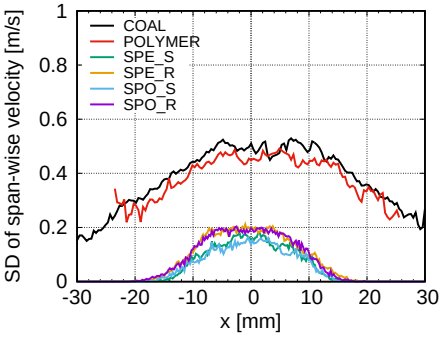

(f) y=150 mm

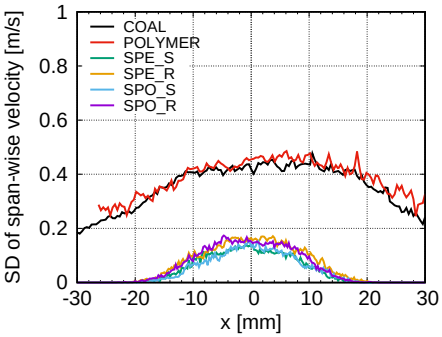

(g) y=180 mm

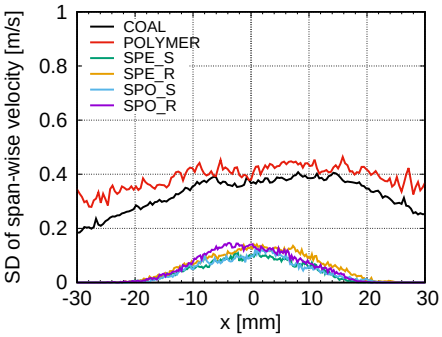

(h) y=210 mm

Figure 4.10: Standard deviation of the radial velocity at different height for all cases.

4.5.2 The particle dispersion

Figure 4.11 shows the instantaneous Mie scattering of the experiment results and the number intensity of the simulation results. Strong luminance means a high concentration of particles. The difference is significant. For the experiment, the strongest luminance appears near the burner for the COAL, but appears at the middle height for the POLYMER. One can notice is that the width of the luminescent part of the COAL is much wider than that of the POLYMER. The POLYMER's strong luminescent part is long and thin. Another thing is that the luminance of COAL monotonically decreases, while the luminance of POLYMER firstly increases and then decreases as heights becoming higher. At the higher height, there is still strong luminance appearing for POLYMER, causing a finger-like structure. This indicates that the COAL's clustering appears near the burner, and it tends to randomly disperse in space at higher height. On the contrast, the POLYMER clusters strongly at the middle height, and also tend to clustering at the higher height. For the simulation cases, the SPE_S and the SPO_S, the SPE_R and the SPO_R have the same look respectively. The look of the number intensity of the SPE_S and the SPO_S is similar to the Mie scattering of the POLYMER. They have the finger-like structures from lower to higher heights, which indicates that the particles clustered there. The look of the number intensity of the SPE_R and the SPO_R is similar to the Mie scattering of the COAL. The finger-like structures are not apparent, which means the particles for these cases are more like to randomly disperse. For the group of G_SPE and G_SPO, it can be noticed that the intensity of G_SPO is little stronger than that of G_SPE. This means the particles with the spheroidal motion model is more clustered than the particles with spherical motion model at some positions.

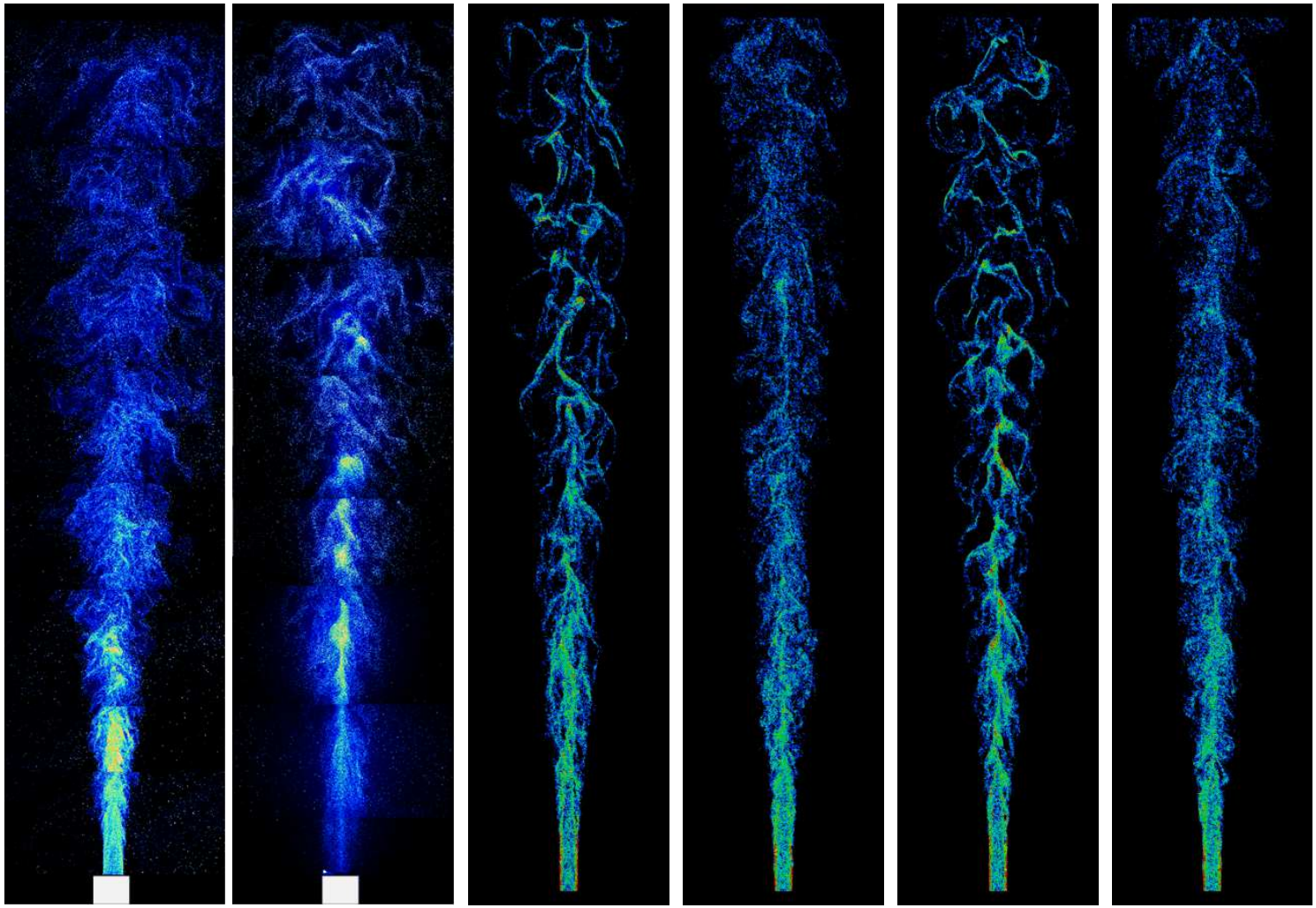

(a) COAL (b) POLYMER (c) SPE_S (d) SPE_R (e) SPO_S (f) SPO_R

Figure 4.11: Mie scattering of the experiment and the particle number intensity of the simulation at instant.

Figure 4.12 shows the averaged Mie scattering of the experimental results and the averaged number intensity of the simulation results. For the experimental results, since the light intensity is not averagely distributed in the laser sheet, the strongest appears at the horizontal centerline, thus the results show a shuttle shaped luminance at each height. Despite this, the trend can be confirmed. Both of the results has a luminescent line at the vertical centerline and outside is dark blue, which means the particles have low probability reach there. The COAL's strongest luminance appears near the burner and monotonically decrease. The POLYMER's strongest luminance appears at the middle height, at lower and higher heights the luminance is weaker. These are the same as the instantaneous results. The simulation results have the same look. All the four simulation results have almost the identical appearance, but still, some differences can be distinguished. The cases with mono-diameter, SPE_S and SPO_S, have two strong number intensities. One at the side near the burner and another at the lower height which is converged by the former makes up an overturning "Y" shape. The cases with diameter distribution, SPE_R and SPO_R, although have strong number intensities at the side near the burner. However, the vertical of the overturning "Y" is not obvious. This shows after injected into space, the trend of the particle clustering of SPE_R and SPO_R becomes weaker as height becomes higher, while the trend of SPE_S and SPO_S increase once and then decrease. On the other hand, the difference between the group G_SPE and G_SPO is not obvious, indicates the particle motion model has a weaker influence than the diameter distribution.

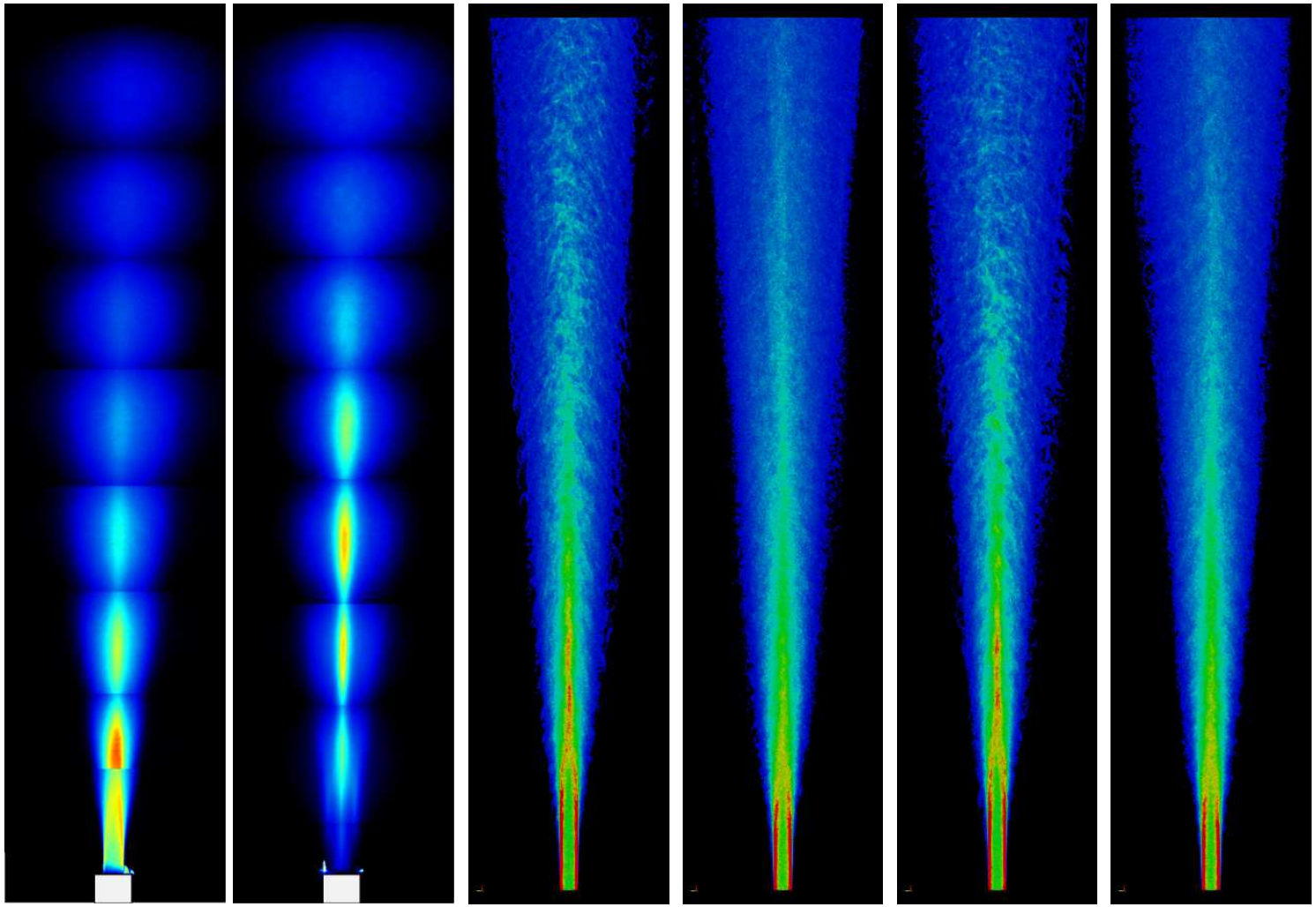

(a) COAL (b) POLYMER (c) SPE_S (d) SPE_R (e) SPO_S (f) SPO_R

Figure 4.12: Time averaged Mie scattering of the experiment and the particle number intensity of the simulation.

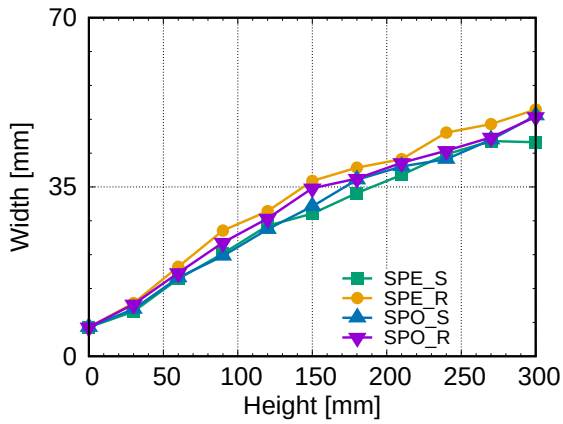

Figure 4.13: The width measured at different heights.

In order to investigate how far the particles are moved, we measured the width of the number intensity of the simulation results, shown in Figure 4.13. The wider the width, the further the particles move. Some differences can be noticed between the group G_SPE and G_SPO. For the SPE_S and SPO_S, the width is not that different at the lower height. However, at middle and higher heights, the width of SPO_S is wider than the SPE_S's width, which indicates that the particles with spheroidal motion model have a trend to move further than the particles with spherical motion model. In contrast, the SPE_R's width is always wider than the SPO_R's, although both of them are wider than the width of mono-diameter cases. This suggests that with the spheroidal motion model, the diameter distribution effect has been weakened.

Figure 4.14 shows the normalized number intensity of the simulation results at different heights, the experimental results are also included. From the middle to the higher heights, the simulation results show a high similarity to the experimental results. At the lower height, since a lot of particles concentrated at the outer side, the number intensity along the centerline becomes small for the simulation results. Still, the difference between the group G_SPE and G_SPO is not distinguished. For the experimental results, except the lower heights, the Mie scattering of the POLYMER is always larger than that of the COAL. The peak of the Mie scattering of the POLYMER is reached at y = 90 mm, while the peak of the COAL's appears at y = 60 mm.

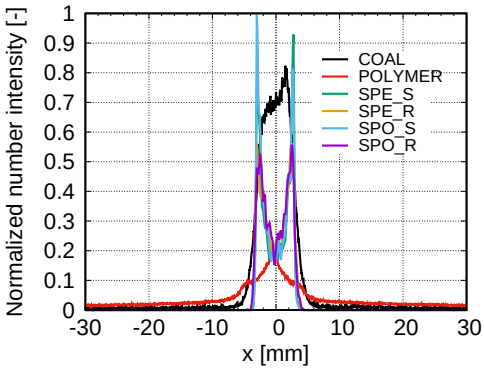

(a) y=20 mm

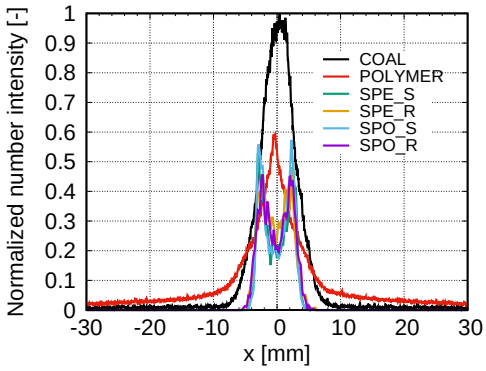

(b) y=30 mm

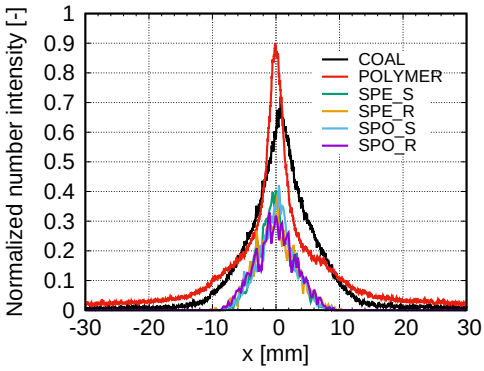

(c) y=60 mm

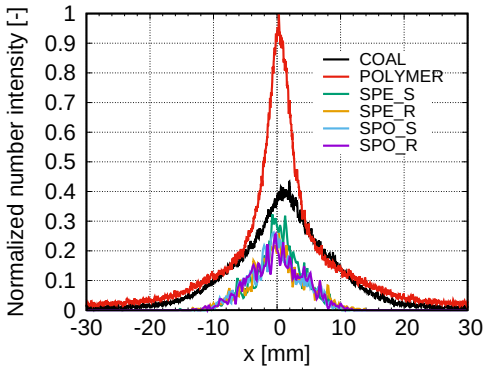

(d) y=90 mm

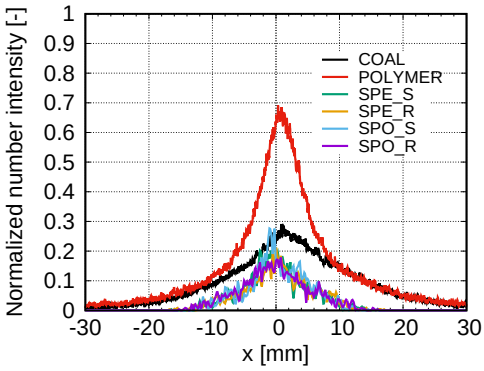

(e) y=120 mm

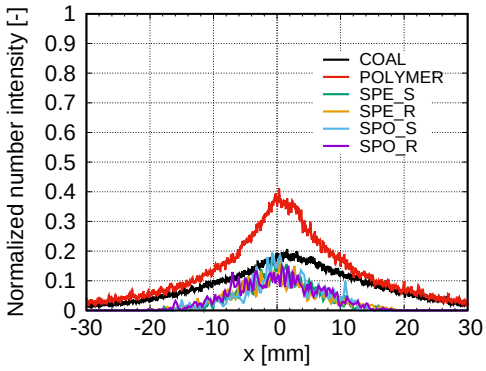

(f) y=150 mm

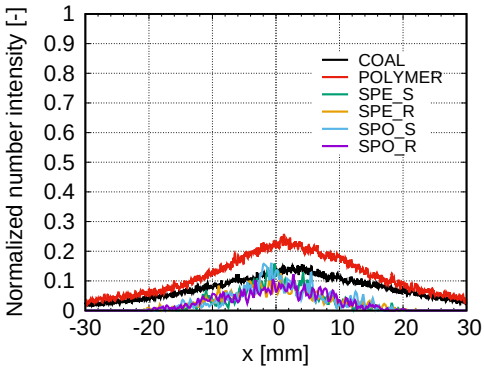

(g) y=180 mm

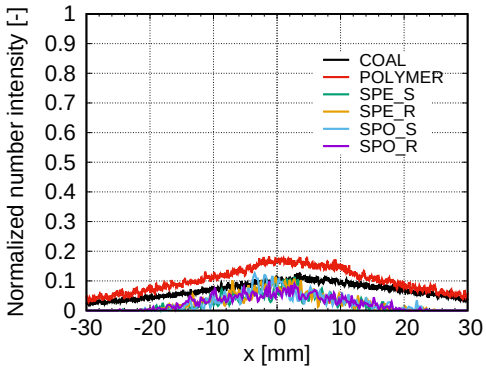

(h) y=210 mm

Figure 4.14: Averaged Mie scattering intensity of the experiment and the number intensity of the simulation at different height.

4.5.3 RDF analysis of the particle distribution

The RDF method mentioned in chapter three is used here to analyze the detail particle dispersion of the simulations. Figure 4.15 shows the RDF results of the simulation cases. The horizontal axis indicates the distance, vertical axis indicates the RDF values. Some differences between the group of G_SPE and G_SPO can be identified. Firstly for the mono-diameter cases, SPE_S and SPO_S, at the lower height such as y = 30 mm, the RDF values of SPE_S and SPO_S are almost the same. As height increasing, the RDF values decrease, and the gap of the difference between the SPE_S and SPO_S becomes apparent. From y = 120 mm, both of the RDF values start to become larger again, and the difference is getting smaller. The results show that from the lower height to the higher height, the case with spheroidal motion model, SPO_S, is more concentrated than the case with spherical motion model, SPE_S. However, the reason of the concentration difference at each height is different. At lower heights, since the particles have just been entrained into space, they have not yet dispersed. Thus the RDF values are large at the lower height. While the height becoming higher, the particles start to disperse, particle pairs that have close distance become less, therefore the RDF values become smaller. But, at the higher height, the particles are fully dispersed in space, which means the particles are completely influenced by the turbulence, and clustering, causing rising RDF values. The close RDF values show that the clustering of the particles of the SPE_S and SPO_S at higher heights is similar.

On the other hand, for the SPE_R and SPO_R, the difference of the RDF values is not significant. Both of these two cases have medium RDF values, much smaller than the SPE_S and SPO_S, indicates that they are more randomly dispersed. And the RDF values monotonically decrease as height becomes higher. The difference between SPE_S and SPE_R is much larger than the difference between SPE_S and SPO_S. And so do the SPO_S and SPO_R. This means the diameter distribution has a much stronger influence on the particles dispersion than the particle shape effect.

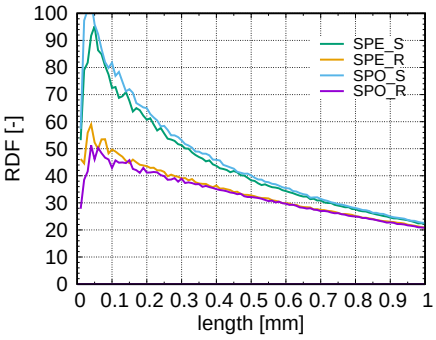

(a) y=30 mm

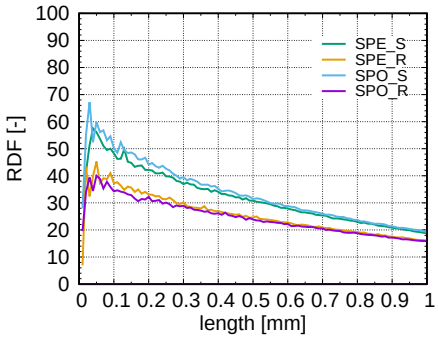

(b) y=60 mm

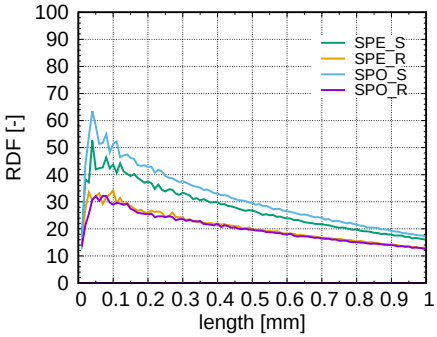

(c) y=90 mm

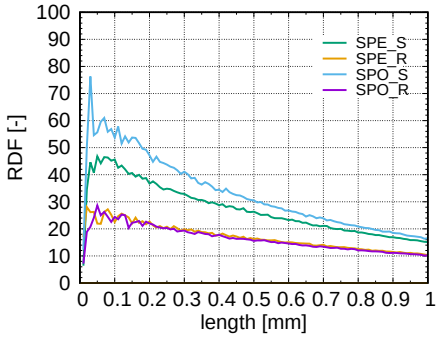

(d) y=120 mm

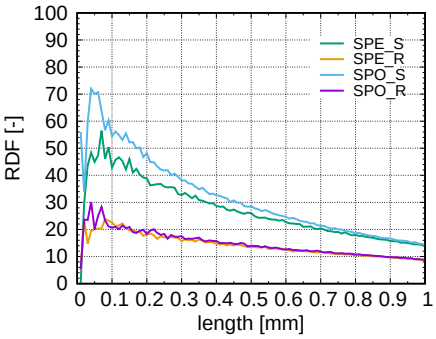

(e) y=150 mm

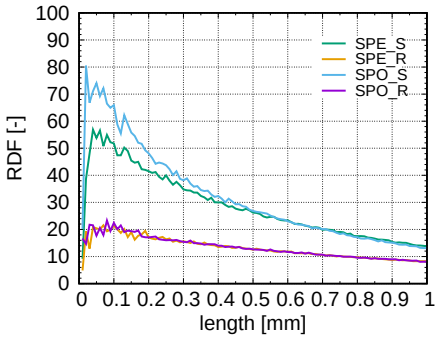

(f) y=180 mm

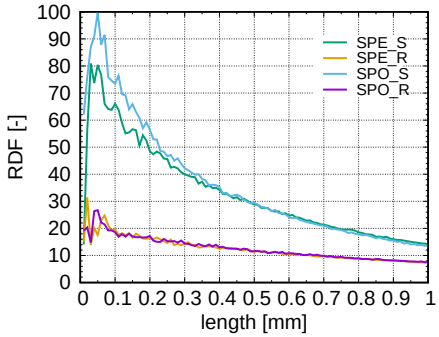

(g) y=210 mm

Figure 4.15: The RDF results at each height.

4.6 Chapter conclusions

In this chapter, an experiment and a simulation are done to investigate the particle's shape effect and diameter distribution effect on the particle's dispersion in a jet burner. the main conclusions are summarized as

1. The particles' velocity profiles of the simulation are in good agreement with the experimental data. However, the influence of the diameter distribution and shape effect are not apparent.

2. By count the particle's number intensity, the Mie scattering look-like results are obtained. The particles dispersion behavior are quite different in the experiment. The simulation results have the same trend and indicate that the difference is mainly caused by the diameter distribution effect.

3. By calculating the RDF values of each case in the simulation, the difference, which is not identified in the velocity and number intensity analysis, is captured. It shows that the diameter distribution effect has a stronger influence on particles dispersion than the shape effect, the same conclusion as the number intensity. The difference between the spherical and spheroidal motion model is identified. The particles with spheroidal motion model are more clustering than the particles with spherical motion model in the mono-diameter cases.

As these conclusions, it suggests that in the jet burner simulations, the diameter distribution effect is much more important than the particle's motion model. However, in the simulations with mono-diameter particles, the particle's motion model will give apparent influence on the results.

CHAPTER 5

A single non-spherical particle's ignition in a vertical uniform flow

5.1 Introduction

As chapter one introduced, coal utilization causes a set of environmental problems, such as atmospheric particulate matter and CO_2 emission. Thus developing a clean coal utilizing technology becomes an urgent matter. The two-phase reacting fields on pulverized coal combustion boilers or coal gasifiers in which a great deal of coal is consumed need a much deeper understanding. However, the pulverized coal combustion is a highly complex phenomenon, including the coal particle's evaporation and devolatilization, its surface reaction, and the gas phase reaction. These phenomena take place interactively at the same time, therefore, it is difficult to make the underlying physics of the governing processes clear. And it is arduous to observe the states inside the boiler or gasifier directly under the extreme temperature and pressure condition. Moreover, the pulverized coal particles have a typical size of the diameter from few tens to hundreds micrometer. The combustion of these particles is quite fast, in few tens millisecond. It is hard to observe a single coal particle's combustion behavior in such limited size and limited time by experiment. Hence multiphase Computational Fluid Dynamics (CFD) becomes a high-powered evaluating and developing tool in pulverized coal combustion field to investigate the coal combustion phenomenon. Lots of efforts, such as Watanabe & Otaka [9], Watanabe, et,

al. [10], Kurose, et,al. [11], Muto, et, al. [12], Hashimoto & Watanabe [13], Hashimoto, et, al. [21], have been done and the coal combustion phenomenon are unraveled gradually. However, all these studies are performed on a large scale that contains a large amount of particles and observe the macro phenomenon of the coal combustion.

Generally in CFD, how to describe the combustion process of a single coal particle is a conundrum. The real coal particle combustion is a complex phenomenon including devolatilization and char combustion. These processes are affected by coal particle's shape, chemical composition, and environment condition. Hence it is hard to model all of these behaviors. In CFD, the particles are commonly assumed to be spherical in order to simplify the mathematical problem and reduce calculation cost. Similar to devolatilization, char combustion and gas combustion processes are enormously simplified. For coal particle's devolatilization, Distributed Activation Energy Model (DAEM) proposed by Anthony [22, 23] is used in general. This model does not consider the chemical structure of coal particle. In order to simplify the problem, it is usually to assume the devolatilization species to be several species or only one imaginary species called $C_aH_bO_c$. The production is determined by experiment in advance, therefore this model can not predict the production in terms of particle's temperature history. Since the devolatilization species is assumed to be an imaginary species $C_aH_bO_c$, the subsequent gas phase reaction is applied by using global reactions. How these simplifications affect the simulation's accuracy is limited in the literature. Despite this, because DAEM needs less initial parameters and global reactions need fewer calculation resources, it is widely used.

Meanwhile, another problem is the lack of observation of a single coal particle's combustion. As the coal particle's combustion is a comprehensive phenomenon and it happens in an instant, it is difficult to observe and to record these procedures. The concrete procedures of coal particle combustion have not been declared clearly. And there are insufficient experimental data to compare with simulation results and to verify the numerical methods.

Fortunately, since the equipment and computer technologies develop rapidly, to catch and record an instant of the coal particle combustion process using a high-speed cam-

era becomes possible. Some of efforts have been done to observe the coal combustion flame and single coal particle burning, like Hwang, et, al. [24], Shaddix & Molina [25], Molina & Shaddix [26]. Recently Lee and Choi from KAIST built an experiment to investigate different composition coal particles' combustion in different concentration of oxygen [27]. They inspected the ignition delay, flame tail and particle burning procedure in detail and discussed the effect of oxygen concentration. Their experiment collected plenty of data that can be used to validate the simulation results and evaluates the numerical methods' precision. On the other hand, abundant coal devolatilization models have been proposed. Some of these new models consider the chemical structure of coal and can calculate the production in terms of particle's temperature history. The most stimulating thing is that some of these models define the devolatilization species in detail, which can be coupled with the detailed reaction mechanism of the gas phase. An increase in high simulation accuracy can be expected in the basic research of coal combustion behaviors.

This chapter investigates a single coal particle's ignition behavior by coupling the Extended-CPD model proposed by Umemoto [28] with gas phase reactions using numerical methods. The work here compares the numerical results with experimental data and tries to reveal a single coal particle's ignition process in detail. In previous works, we found that a spheroidal particle's motion behavior is similar to the coal particle's than a spherical particle's (see Zhang, et, al [7]). Hence this work uses a spheroidal particle instead of the spherical particle to examine the particle's ignition behavior. In the first stage, this work uses Extended-CPD model to calculate the volatile velocity but assumes the volatile species to be methane and applies global reactions to gas phase reaction to reduce calculation cost.

5.2 Numerical methods

5.2.1 Governing equations

In this chapter, the ALE method is used to calculate a single particle's motion. The governing equations of the gas phase of ALE method are expressed as

$$\frac{\partial \rho_f}{\partial t} + ((\boldsymbol{u} - \boldsymbol{u}') \cdot \nabla)\rho_f = -\rho_f \nabla \cdot \boldsymbol{u}, \tag{5.1}$$

$$\frac{\partial \boldsymbol{u}}{\partial t} + ((\boldsymbol{u} - \boldsymbol{u}') \cdot \nabla)\boldsymbol{u} = -\frac{1}{\rho_f}\nabla p + \frac{1}{\rho_f}\nabla \cdot \sigma + \boldsymbol{g}, \tag{5.2}$$

$$\frac{\partial h}{\partial t} + ((\boldsymbol{u} - \boldsymbol{u}') \cdot \nabla)h = \frac{1}{\rho_f}\nabla \cdot (D_h \nabla h). \tag{5.3}$$

where ρ_f and $\boldsymbol{u}$ are the fluid density and velocity, respectively, $\boldsymbol{u}'$ is the mesh velocity, p is the pressure, σ is the surface stress tensor, D_h is the enthalpy diffusion coefficient, and h is the total enthalpy. The ALE method is equivalent to the Lagrangian method when $\boldsymbol{u}' = \boldsymbol{u}$ but is equivalent to the Eulerian method when $\boldsymbol{u}' = 0$. We apply a particle's velocity $\boldsymbol{v}$ to $\boldsymbol{u}'$. Thus the slip velocity $\boldsymbol{u} - \boldsymbol{v}$ is generated between the fluid and the particle, which depends on the pressure and friction force distributions on the particle's surface. This means that the entire mesh around a single particle rotates and oscillates due to the variations in the pressure and friction force distributions. The six degrees of freedom motion of a particle in a fluid flow can be performed by this procedure.

The particle's velocity is governed by the equation shown as

$$\rho_p V_p \frac{d\boldsymbol{v}}{dt} = \boldsymbol{F}_D + \boldsymbol{F}_B, \tag{5.4}$$

where ρ_p, V_p and $\boldsymbol{v}$ are the density, volume, and velocity of the particle, respectively. F_D and F_B are the drag force and buoyancy respectively. The drag force F_D in this paper is calculated by summing the contributions of friction and pressure as

$$\boldsymbol{F}_D = \boldsymbol{F}_{Dprs} + \boldsymbol{F}_{Dfrc} = -\int_S p\boldsymbol{e}_y \cdot \boldsymbol{n} dS + \int_S \boldsymbol{n} \cdot \tau \cdot \boldsymbol{e}_y dS, \tag{5.5}$$

where $\boldsymbol{n}$ is the surface normal vector, p is the pressure, τ is the stress tensor, and $\boldsymbol{e}_y$ is the direction of particle's motion.

The particle's surface temperature is calculated as

$$m_{p,v} C_p \frac{dT_p}{dt} = Q_{conv} + Q_{rad} + Q_{reac} \tag{5.6}$$

$$Q_{conv} = \int_S h_{conv}(T_f - T_p) dS \tag{5.7}$$

where C_p is the specific heat capacity, and T_p is the particle's surface temperature. $m_{p,v}$ is the particle mass used for the volatile gas calculation. It decreases as the particle blows out volatile gas, differs from the constant ρ_p used to calculate the particle inertia in Equation (5.4). Q_{conv}, Q_{rad} and Q_{reac} are the heat transferred between the fluid and the particle via convection, radiation, and particle surface reaction respectively. This paper simulates one particle in space thus the radiation heat Q_{rad} is neglected. No particle surface reaction is considered thus Q_{reac} is set to be 0. h_{conv} in Equation (5.7) is the heat transfer coefficient of the gas phase.

5.2.2 Chemical reaction modeling

In this paper, the volatile gas blows out from the particle's surface. The velocity of the volatile gas is calculated by Extended-CPD (extended chemical percolation devolatilization) model. Different from the usual coal devolatilization model, for instance, Flash-Chain model [29, 30], FG-DVC model [31] and original CPD model [32–34], the Extended-CPD model defines the specific species of volatile gas. In the Extended-CPD model, the composition of the light gas is defined as CO, CO_2, CH_4 and H_2O, while the composition of tar is defined as benzene, naphthalene and phenanthrene (see Umemoto, et, al. [28] in detail). The amount of each devolatilization species blown out will vary in terms of the temperature history. Therefore it is possible to calculate gas phase reactions using a detailed reaction mechanism based on the explicit definition of the composition of the volatile gas. However, in order to reduce the calculation cost, the volatile gas blown out by the particle is assumed to be methane and a simple two-stage global reaction is applied in this chapter. The reactions are

$$2CH_4 + 3O_2 = 2CO + 4H_2O \tag{5.8}$$

$$2CO + O_2 = 2CO_2 \tag{5.9}$$

The procedure of calculating velocity of the volatile gas is given below.

Firstly maintain the temperature and the mass for each grid point on the particle's

surface.

Secondly update the temperature of each grid point using Equation (5.6) and (5.7).

Next, calculate the volatile mass in terms of the grid point's temperature and mass, and then update the mass of the grid point. It is shall be noted that at this time the volatile mass is contributed by CO, CO_2, CH_4, H_2O, benzene, naphthalene and phenanthrene.

Next regard the composition of volatile gas as methane and convert the mass to methane's volume.

Finally calculate the volatile gas velocity in terms of the methane's volume, grid area and grid normal vector.

Because the temperature is kept and calculated by each point itself, thus a temperature distribution will appear on the particle's surface.

5.2.3 Flame index

Flame index FI is defined as

$$\mathrm{FI} = \nabla Y_{fuel} \cdot \nabla Y_{O_2} \tag{5.10}$$

FI is the dot product of the gradients of fuel and oxidizer. It is used to distinguish between premixed flames and diffusion flames [35]. A positive value of FI indicates that the fuel and oxidizer are premixed thus a premixed flame is formed. On the contrary, a negative value of FI means it is a diffusion flame. In this chapter, FI is not only used to distinguish between premixed flames and diffusion flames but also used to identify premixed regions and diffusion regions of the mixture gas before ignition.

5.3 Computational details

Figure 5.1 shows the schematic of the simulation. Uniform hot gas with 1273K temperature flowed upwards with a velocity of 1 m/s. The hot gas was assumed to be air, composed of 79% N_2 and 21% O_2. The particle was injected into the hot gas flow horizontally

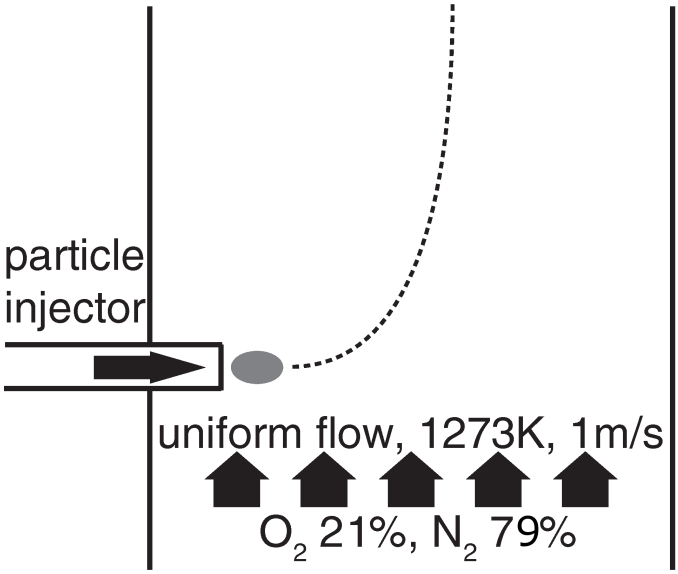

Figure 5.1: Schematic of simulation.

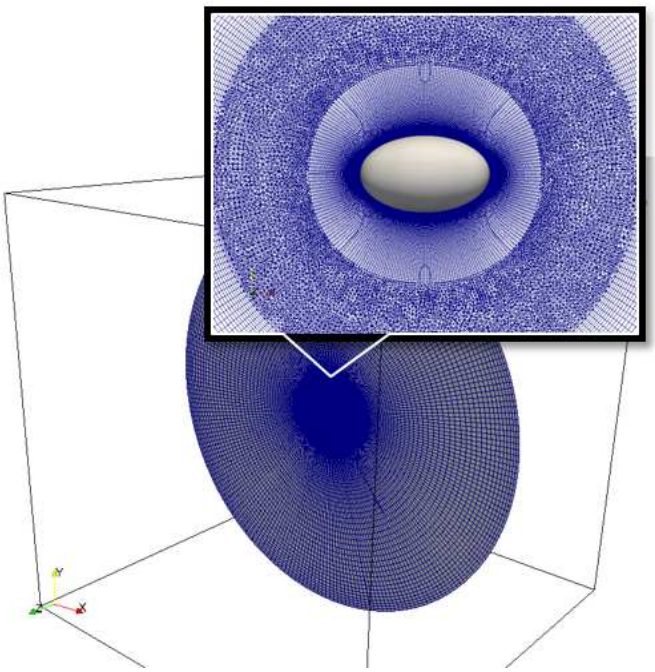

Figure 5.2: Calculation domain and particle shape.

Table 5.1: The property of the spheroidal particle used in this chapter.

Density [kg/m^3]	1500
Diameter a [μm]	60
Diameter $b = c$ [μm]	35.5
Initial orientation [°]	0
Sphericity [-]	0.957

and heated. The initial temperature of the particle was 373K and the initial velocity was 1.5 m/s. All these configurations satisfied the experiment done by Lee & Choi [27].

As previous research (Zhang, et, al. [7]), it was found that a spheroidal particle has a much similar motion with coal particle rather than a spherical particle. Specifically, a coal particle with complex shape will rotate in a flow. The spheroidal particle can have the rotation behavior as coal particle, while the spherical particle can not. For the drag coefficient, when a coal particle rotates, the particle's drag coefficient curve oscillates. The spheroidal particle's drag coefficient curve also oscillates, similar to the coal particle. However, the spherical particle's drag coefficient has no oscillation, not like the coal particle and the spheroidal particle. Hence we considered it was better to use a spheroidal particle instead of a spherical particle to investigate the coal particle's behavior. We used a spheroidal particle with a sphericity of 0.96. The property of the particle was listed in table 5.1. Initial orientation was the angle between the spheroid's major axis and the horizontal plane.

The particle was placed in the upward flow at the beginning of the computation. At the beginning, the particle was fixed forcibly until 40000 steps. During this time, the uniform hot flow was built and stabilized. After that, the particle was released, and the six freedoms of the calculation started. While releasing the particle, a horizontal initial velocity of 1.5 m/s was given to simulate the injection. The calculation domain was shown

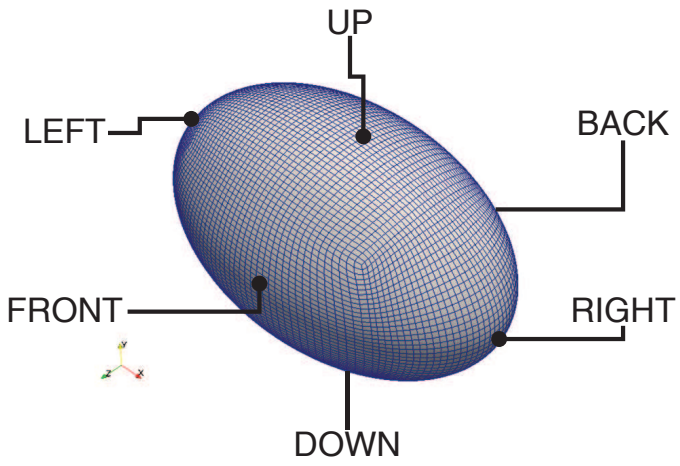

Figure 5.3: Six tracking points are chosen.

in Figure 5.2.

When the particle was released, the temperature distribution was uniform, 373K. After the particle was heated, a temperature distribution appeared over the particle's surface. In order to trace the temperature variation, six points on the surface were chosen. These points were evenly distributed on the surface and were the most representative points. The points were shown in Figure 5.3.

The parameters needed for Extend-CPD model were listed in table 5.2. All these properties were kept by each grid point over the particle's surface during the calculation.

5.4 Results and discussion

5.4.1 Particle surface temperature and volatile velocity

Figure 5.4 shows the temperature variation of the six tracking points chosen over the particle's surface. The initial temperature of each point is 373K. After the particle's release, the temperature grows as heat transfers from the fluid to the particle. The temperature of the two particle heads (LEFT and RIGHT) is about 100K higher than the temperature of the particle body. The RIGHT has the highest temperature and the LEFT's temperature is a little lower. The UP has the lowest temperature on the surface. The FRONT and BACK

Table 5.2: The parameters needed for the Extend-CPD model. Here the unit of NMR analysis indicates how many chemical bonds in one mole bonds. Ar represents the aromatic ring.

Elemental analysis	C	%	83.26
	H	%	4.30
	O	%	11.49
	N	%	0.30
	S	%	0.64
NMR analysis	Ar-CH_2-CH_2-Ar	mol/mol	0.160
	Ar-CH_2-CH_2-Ar	mol/mol	0.000
	Ar-Ar	mol/mol	0.000
	Ar-O-Ar	mol/mol	0.415
	Ar-CH_2-Ar	mol/mol	0.000
	Ar-COOH	mol/mol	0.105
	Ar-OH	mol/mol	0.196
	Ar-CH_3	mol/mol	0.088
	Ar-H	mol/mol	0.462
aromatic ring ratio	1 ring	%	23.2
	2 ring	%	10.3
	3 ring	%	66.5
	4 ring	%	0.00

have a temperature between the UP's and DOWN's. This can be understood because the particle is injected into the hot flow with an initial velocity towards the right direction. Thus the RIGHT hit the hot flow directly and has the highest temperature. For the LEFT, since the particle rotates counterclockwise, the LEFT hits the hot flow from the bottom side thus its temperature also becomes higher. Due to the hot fluid separates from the upside of the particle, the UP has the lowest temperature. At about 4ms, the temperature of all points suddenly increases. It is considered that the particle ignites at this moment.

Figure 5.5 shows the volatile velocity at the surface of the six tracking points. The line colors in this figure correspond to that of Figure 5.4. The sequence of the velocity magnitude is the same as the sequence of the temperature. The volatile starts to been released while the particle surface temperature is greater than about 800K. At the beginning, the volatile velocity of the RIGHT and LEFT is much larger than that of the other 4 points. From about 3.5ms, the volatile velocity of the RIGHT and LEFT becomes constant, while other points' velocities are still increasing. That is because, in the Extended-CPD model, the volatile mass is only affected by temperature, mass, and the mass composition. The RIGHT and LEFT release more volatile gas out than other points and have a faster decrease in mass. At about 3.5ms, the effects of temperature increase and mass decrease to the volatile velocity reach a balanced state, thus the velocities of these two points become constant. At about 4ms, because the temperature suddenly increases, all the volatile velocities suddenly increase at the same time.

5.4.2 Comparing with experimental result

Figure 5.6 and 5.7 show the experimental results of Lee & Choi [27]. They show the ignition delay of the particle and the tail flame incline angle respectively.

In this chapter, the particle size is 60 μm and the oxygen concentration is 21%. In Figure 5.6, the particles with a diameter of 75-90 μm ignites at about 4.5ms while the oxygen concentration is 21%. The figure also shows that the ignition delay decreases while the particle size becomes smaller. Hence the particle with a size of 60 μm shall ignite within 4.5ms. The simulation results show that the particle ignites around 4ms,

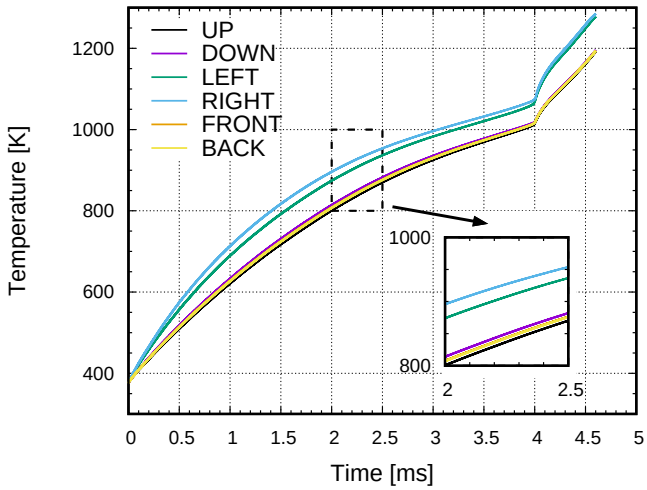

Figure 5.4: The temperature variation of the six tracking points.

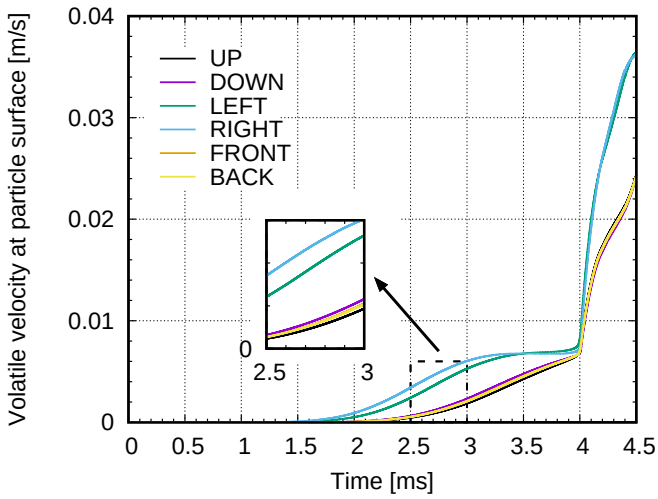

Figure 5.5: The volatile velocity of the six tracking points.

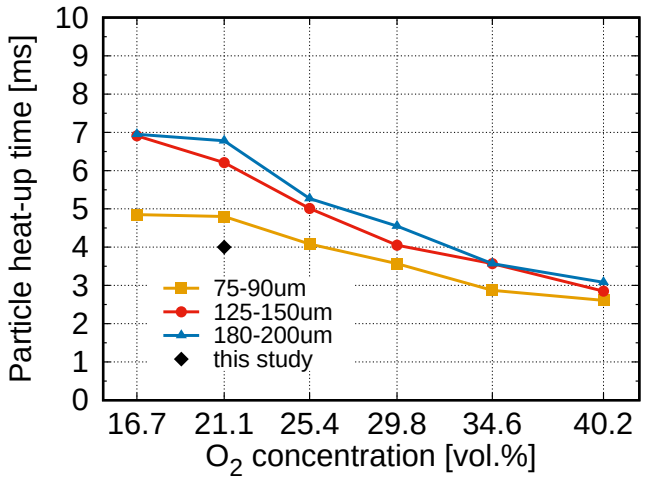

Figure 5.6: The ignition delay of the experimental. The diamond mark represents the simulation result.

which is in good agreement with the experiment.

Due to the slip velocity generated between the particle and the hot flow, the flame around the particle inclines. The inclined angle of the flame in this work is about 50 degrees. The flame inclined angle is related to the slip velocity between the particle and the hot flow. For the experimental result shown in Figure 5.7, the flame inclined angle is plotted against the velocity ratio which is the ratio of coal particle carrier gas velocity versus the hot flow velocity. In their experiment, the coal particle's velocity is not measured. At the instant while the coal particle is injected into the flow, the velocity of the particle is not exactly the same as the carrier gas velocity. We found that in their experiment a coal particle's velocity is in a range of 0.9m/s and 1.1m/s, while the carrier gas velocity is in the range of 1.3m/s and 2.7m/s. This leads to a slip velocity range from 0.2m/s to 1.8m/s. Therefore the particle with an initial velocity of 1.5m/s in this work has the velocity ratio range from 1.7 to 3.3. In Figure 5.7, by considering the slip velocity, the minimum, maximum and mean values of this work are plotted. It shows that the simulation result of an inclined angle of 50 degrees is in good agreement with the experimental result at the mean velocity ratio. It is confirmed that the simulation result is accurate.

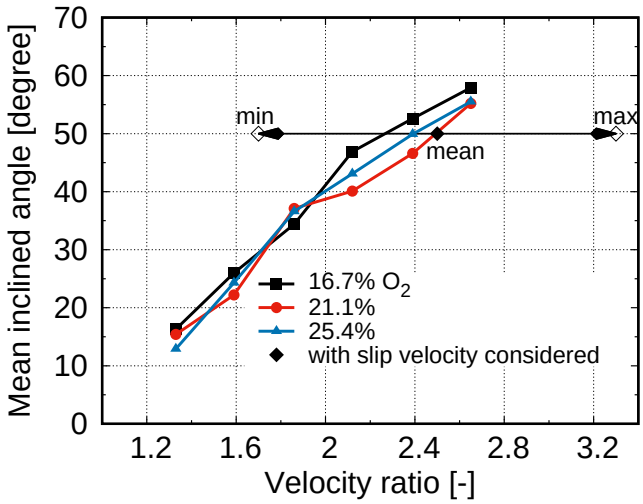

Figure 5.7: The flame inclined angle of the experimental and simulation data. The velocity ratio in the experiment is the ratio between the particle carrier gas and the hot flow. The diamond mark represents the simulation result.

5.4.3 Mixture gas formation before ignition

Figure 5.8 shows the premixed and diffusion regions' development around the particle. A pink color indicates the premixed region and a white color indicates the diffusion region. The green color represents FI=0. Figure 5.9 shows the premixed and diffusion regions' development and the corresponding temperature distribution. Only temperatures higher than the environmental temperature 1273K are shown, which means temperatures lower than 1273K are shown in white color. The black line overlaps with the temperature represents FI=0, which shows the boundary of the premixed and diffusion regions.

After the particle is released and heated, as Figure 5.4 shows, the two heads of the particle have the highest temperatures compared with other points, the volatile gas starts to blow out from these parts. A tiny premixed region appears near the right head of the particle, shown in Figure 5.8(a). At 1.5ms, it clearly can be seen that a premixed region has formed around the particle, and outside is a thin diffusion region (Figure 5.8(b)). While these two regions are expanding, the diffusion region has a faster expansion rate, according to Figure 5.8(c) and 5.8(d). The premixed region inside becomes inclined towards the up-left side behind the particle. Its shape looks spherical but has the particle located

at the bottom-right boundary of it (shown in Figure 5.8(c) and 5.9(b)). This is because relative to the particle, the fluid is flowing towards the up-left side and the stagnation point appears at the bottom-right side of the particle. Thus the premixed region won't expand to the front side of the particle but expands to the rear side. The diffusion region expands but keeps its spherical shape (Figure 5.8(c), 5.8(d) and 5.9(b)).

From 3ms to 3.5ms, the two regions keep their size and stop propagation. However, the rear parts of them become smaller and both become elliptical (Figure 5.9(d)). Reference to the temperature shown in Figure 5.9(a) and 5.9(c), a high-temperature region, where the temperature is higher than the environmental temperature 1273K, appears at the rear boundary of the premixed and diffusion regions. This high-temperature region appears at about 2.5ms and expands. At about 3ms, the high-temperature region becomes ring-shaped and encircles the particle, shown in Figure 5.9(a). At that time, the temperature with pale blue color around the particle is only a little higher than 1273K. This high temperature expands slowly and rises a little at 3.5ms, shown in Figure 5.9(c).

This behavior can be explained as that while the particle is releasing the volatile gas, the concentration gradients of methane and oxygen are formed, as shown in Figure 5.12. All plots are plotted along the white line shown in Figure 5.12(a). As the plot passes through the particle, there are no data at the particle location thus there is a gap at the center of each plot. It is obvious that the mole fraction of methane becomes smaller and the mole fraction of oxygen becomes larger away from the particle. Because the particle's surface temperature is lower than environmental temperature 1273K, a temperature gradient appears. The temperature becomes higher when away from the particle. Figure 5.12(b) shows the mole fraction of the gas and the gradient of temperature at 2ms. For the existence of the methane and oxygen, the reaction occurs although it is very slow. At the boundary of the premixed and diffusion regions, the concentration of methane and oxygen has a better ratio and the temperature is high enough. Outside the boundary, although the temperature is higher and oxygen is rich, the concentration of the methane is too low thus the reaction becomes slow. Inside the boundary, the concentration of the methane is high but the temperature is not high enough thus similar reaction becomes slow. Since the re-

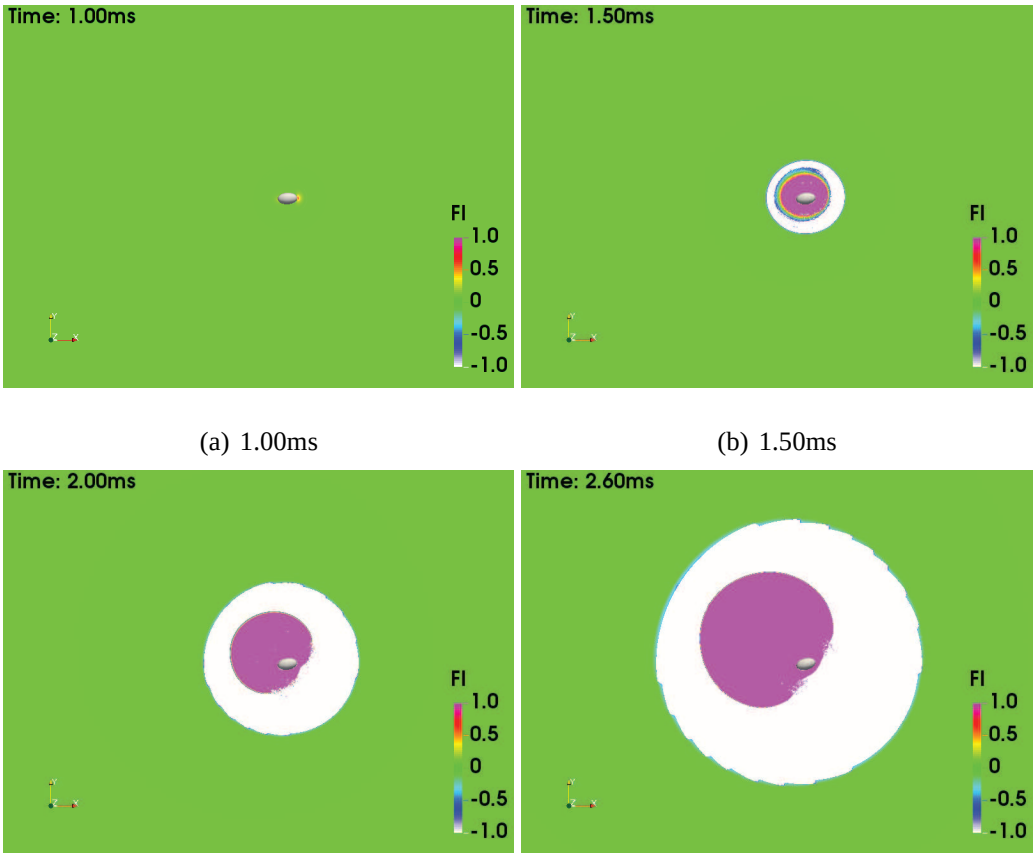

(a) 1.00ms (b) 1.50ms

(c) 2.00ms (d) 2.60ms

Figure 5.8: The premixed region and diffusion region identified by FI. Green area is FI = 0.

action has the fastest reaction rate at the boundary of the premixed and diffusion regions, the heat accumulates faster than other places. As the result, the high-temperature region appears at the boundary of the premixed and diffusion regions. From Figure 5.12(c), as the high temperature appears, the reaction becomes faster and oxygen is consumed faster than other places, thus a hollow of oxygen concentration appears at the boundary.

5.4.4 Ignition behavior

Figure 5.10 and 5.11 show the premixed and diffusion flames' development and the corresponding temperature distribution. Here since the high-temperature region appeared and the gas phase is ignited, the FI identifies the premixed and diffusion flames. The black

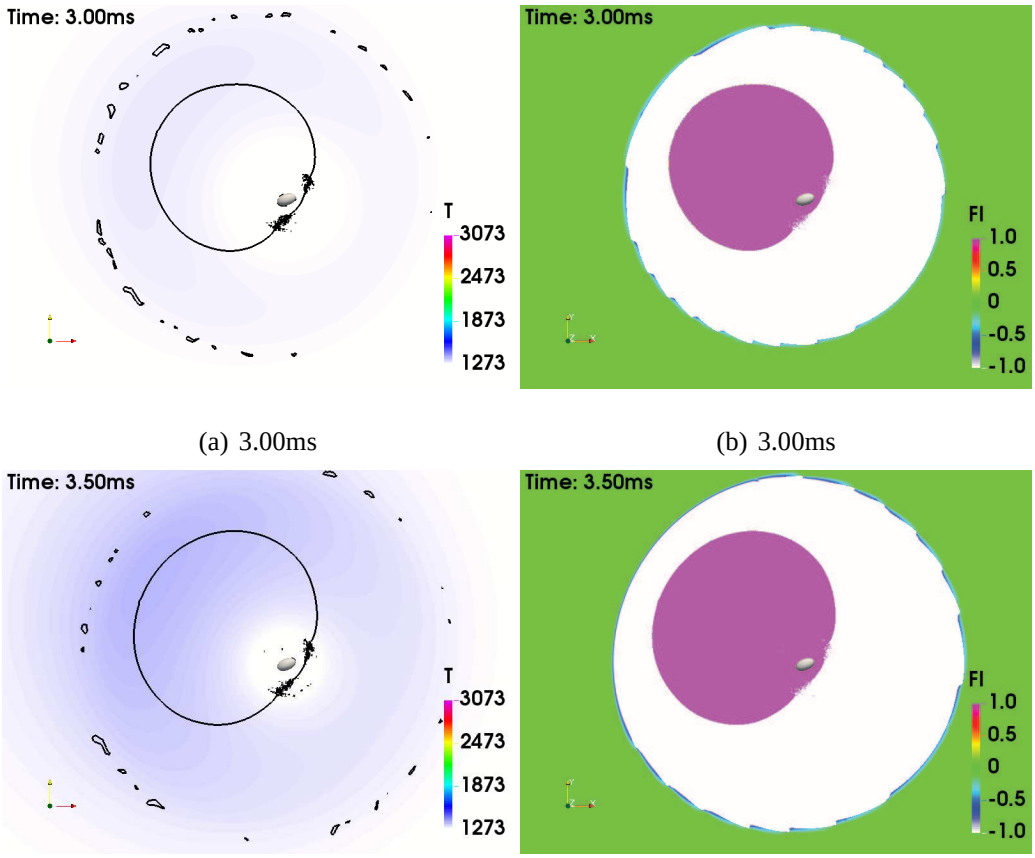

(a) 3.00ms (b) 3.00ms

(c) 3.50ms (d) 3.50ms

Figure 5.9: The premixed region and diffusion region identified by FI and corresponding temperature distribution. Green area and black line represent FI = 0.

line of FI=0 indicates the boundary of the premixed and diffusion flame.

From Figure 5.10(a), the high-temperature region which appeared before ignition becomes larger and expands towards the particle, and its temperature gets higher. Compared to Figure 5.9(c) at 3.5ms, the region with the highest temperature moves toward the particle because the particle side has a richer concentration of methane. During that time, due to the methane and oxygen consumption, both premixed and diffusion flames become smaller from the rear, show in Figure 5.10(b). At 3.99ms, the temperature grows rapidly and its area expands larger. However, the highest temperature region stops moving to the particle but elongates itself to both sides of the particle, as shown in Figure 5.10(c). This is because of the volatile gas blow-out effect. The volatile gas is blown out from the particle's surface and pushes the flame away from the particle. Figure 5.10(d) shows the same tendency, that the premixed and diffusion flames behind the particle stop getting smaller and keep their thickness. The premixed flame becomes slender and the diffusion flame seems to disappear at point A and B. At 4ms, the high-temperature region has a trend to swallow the particle up and the highest temperature is nearly 3000K, indicates that the reaction is violent, given in Figure 5.10(e). The flame in Figure 5.10(f) shows that the diffusion flame separates into two parts by the premixed flame at point A and B (Figure 5.10(f)). The front part of the diffusion flame keeps its round shape and the rear part keeps its position. Figure 5.11(a) shows the moment when the flame encircles the particle. The high-temperature region almost swallows the particle up. The diffusion flame has a trend to cut the premixed flame and surround the particle from point A and B, shown in Figure 5.11(b). At 4.02ms, both premixed and diffusion flames separate into two parts. Around the particle, a premixed flame is formed and outside is the diffusion flame. Both flames are round shaped. On the bottom-right side, there are the remain parts of the premixed and diffusion flames, and these two parts are located at the outside boundary of the high-temperature region, show in Figure 5.11(c) and 5.11(d). These two parts finally disappear as the reaction continues at 4.6ms. The premixed flame around the particle also disappears since the oxygen inside the flame is totally consumed and its concentration becomes zero, therefore inside the diffusion flame, the FI becomes zero.

The highest temperature around the particle decreases because the oxygen concentration is not rich enough. However, the diffusion flame propagates and its size becomes quite large. Finally, the diffusion flame reaches a stable state, which is shown in Figure 5.11(e) and 5.11(f).

Figure 5.12(d) and 5.12(e) show the gas mole fraction and temperature gradient when the gas phase is ignited. After the gas phase is ignited, the temperature becomes extremely high and correspondingly the oxygen mole fraction becomes lower. Finally, the oxygen inside becomes zero and the temperature decreases (plotted in Figure 5.12(f)).

This procedure explains the sudden increase in temperature and volatile velocity shown in Figure 5.4 and 5.5 which appears at about 4ms. At that time, the volatile gas around the particle is ignited at the up-left side behind the particle. The flame propagates toward the particle thus the particle surface temperature increases fast. This high temperature also causes a rapid increasing of volatile velocity.

5.5 Chapter conclusions

This paper reports a direct numerical simulation of the ignition of a single particle freely moving in a uniform flow. The particle has volatile gas blowing out from the surface. The volatile velocity is calculated using Extended-CPD model and its composition is assumed to be methane. The particle's heating, devolatilization, ignition and burning processes are caught and discussed. It is found that after the particle is heated and started to release devolatilization species, a premixed and diffusion regions are formed around the particle. These two regions are concentric and the diffusion region is outside. The gas phase is ignited at the boundary between the premixed and diffusion region at the rear of the particle. The flame propagates fast and encircles the particle in a moment thus the temperature of particle's surface rises rapidly. This leads to the sudden increase of the volatile velocity on the particle surface. The ignition time and the flame inclined angle show a good agreement with that of experimental results.

In the future, a similar simulation with a fully functioned Extended-CPD model cou-

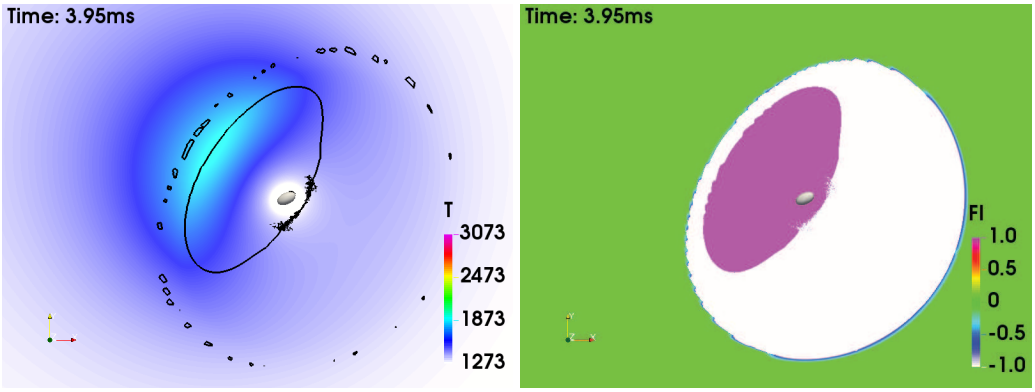

(a) 3.95ms

(b) 3.95ms

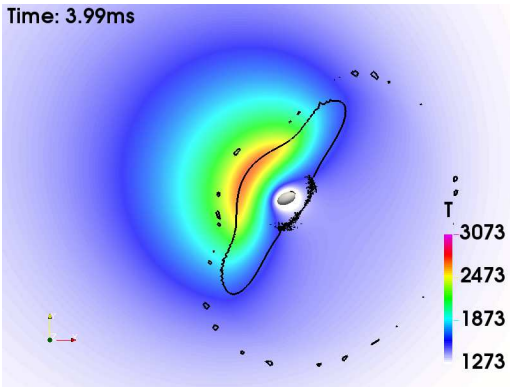

(c) 3.99ms

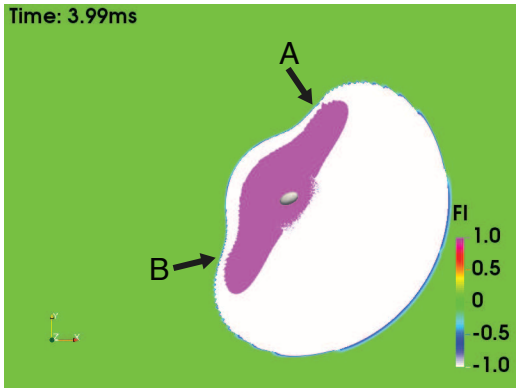

(d) 3.99ms

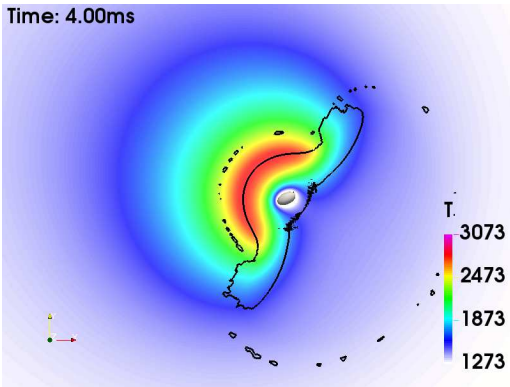

(e) 4.00ms

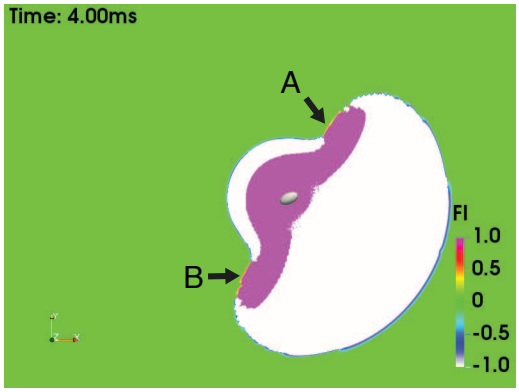

(f) 4.00ms

Figure 5.10: The premixed flame and diffusion flame identified by FI before 4ms. Green area is FI = 0.

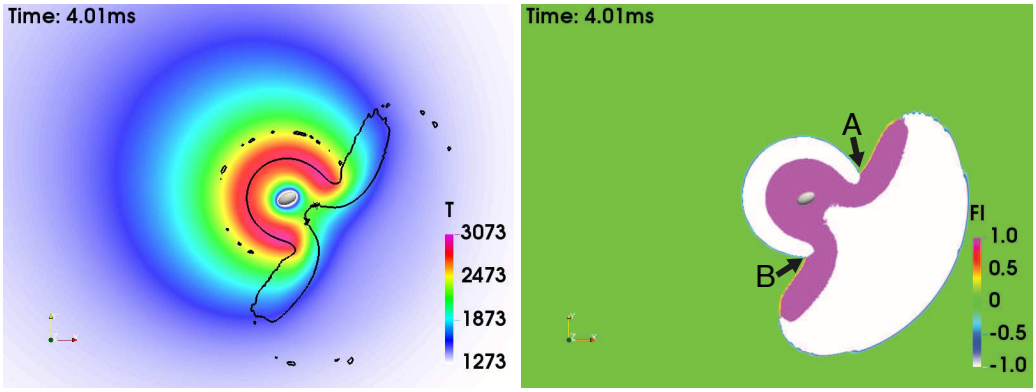

(a) 4.01ms

(b) 4.01ms

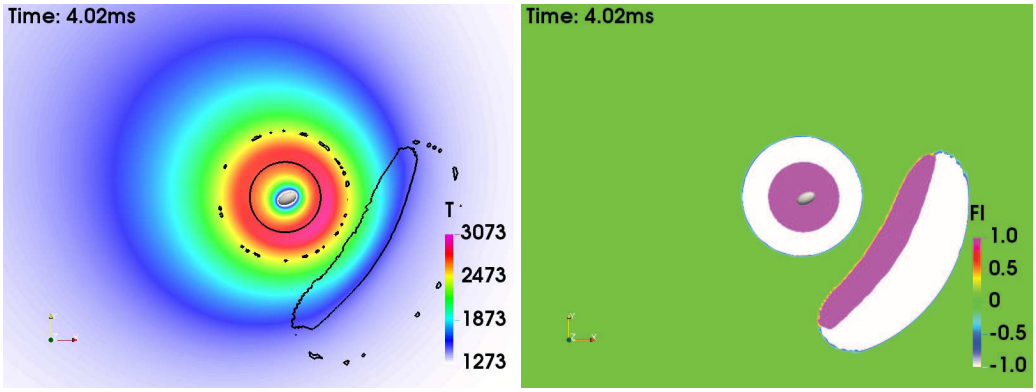

(c) 4.02ms

(d) 4.02ms

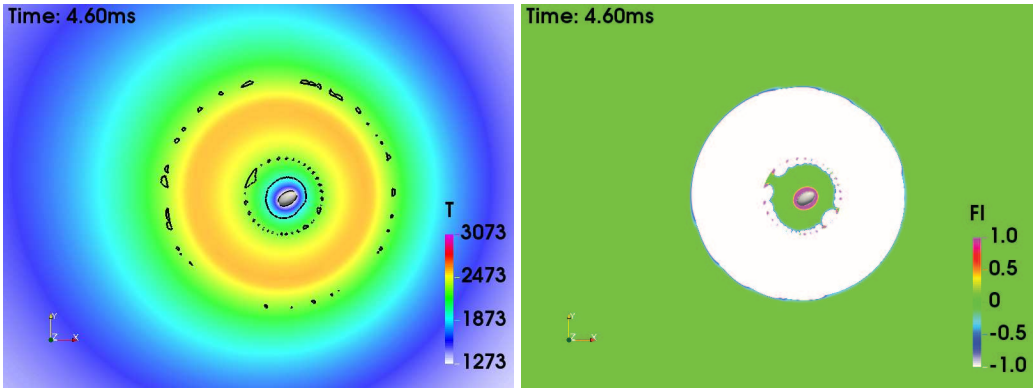

(e) 4.60ms

(f) 4.60ms

Figure 5.11: The premixed flame and diffusion flame identified by FI after 4ms. Green area is FI = 0.

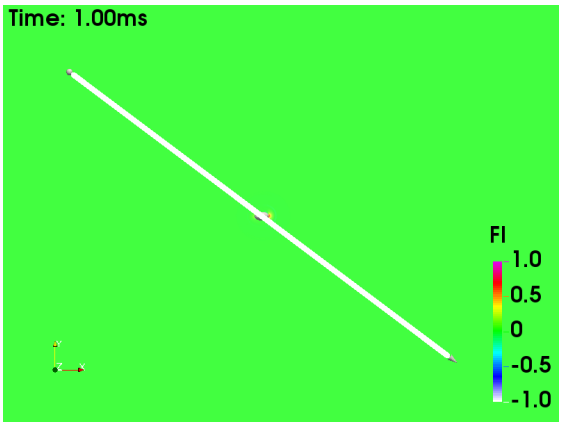

(a)

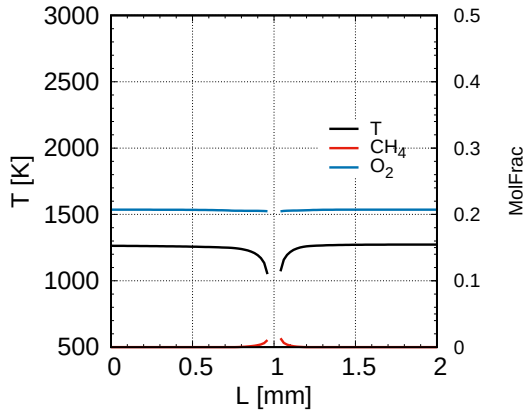

(b) 2.00ms

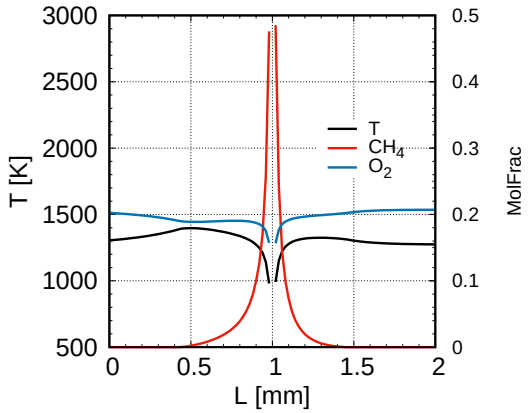

(c) 3.50ms

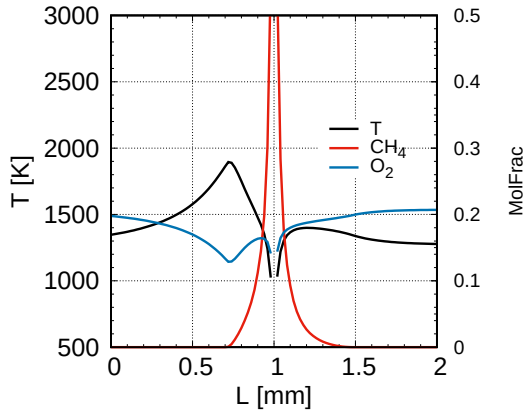

(d) 3.95ms

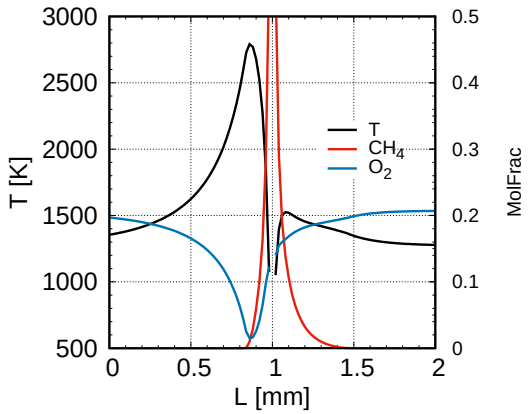

(e) 4.00ms

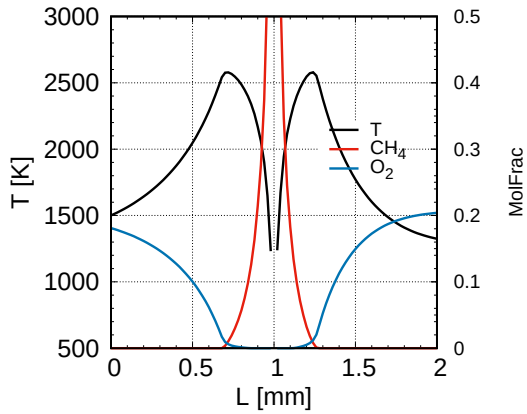

(f) 4.60ms

Figure 5.12: The concentration variation of methane and oxygen. Temperature is also shown in it. (a) shows the white line where the data sampled. The sample line length is 2 mm, particle is located at the center, thus the points at 1 mm do not have data.

pling with the detailed reaction mechanism will be performed. And not only the spheroidal particle but also the spherical particle and the coal particle with a complex shape will be applied to the simulation in order to investigate the shape effect on the particle's ignition.

CHAPTER 6

Conclusions and suggestions

6.1 Conclusion of the dissertation

In this dissertation, we mainly study the particle's shape effect on the particle's dispersion behavior in the turbulent flow. The most outstanding contribution of this dissertation is a new spheroidal particle motion model is proposed and validated. This model is made based on the numerical simulation of six degrees of freedom motion of a single spheroidal particle. We found the spheroidal particle's $C_D - Re$ curves oscillated between a limited upper and lower band. After taking the PDF, it is the same as the sine curve's PDF. Therefore, we made the spheroidal particle motion model using the form of the Equation (2.4) and the sine function. The model is written as

$$\log_{10} C_D = \log_{10} C_{Dmin} + (\log_{10} C_{Dmax} - \log_{10} C_{Dmin}) * \frac{sin(2\pi\theta)+1}{2}, \tag{6.1}$$

where θ is a random number between 0 and 1, represents the spheroidal particle's rotation angle. In this solution, 0.75 means the particle is vertical, and 0.25 means the particle is horizontal. C_{Dmax} and C_{Dmin} are represent as

$$C_D = \begin{cases} \frac{24}{Re}(1 + A * Re^{B - C * \log_{10} Re}), & 0.01 < Re \leq 10 \\ \frac{24}{Re}(1 + X * Re^{Y}), & 10 < Re \leq 100 \end{cases} \tag{6.2}$$

where A, B, C, X, and Y are the parameters that are determined by the six degrees of freedom for the particle's motion.

This model is compared with the empirical spherical motion model in chapter three. The shape influence on the particles' dispersion in the isotropic turbulent flow is studied. The isotropic turbulent flow is maintained to keep its turbulent strength and the particles' dispersion is statistically analyzed using D-value method and RDF method. The results are organized in terms of the Stk number and demonstrate that the particles' shapes do affect the particles' dispersion behavior.

Since the particle's motion behavior is markedly affected by the shape, thus in the large-scale simulations of the coal combustion field which have a large amount of particles dispersing may lead to inaccurate results. In chapter four, we performed both an experiment and a simulation of particles' dispersion of a real scale jet burner. The same as chapter three, the newly proposed spheroidal and empirical spherical particle motion model is used. Simultaneously, the particle's diameter distribution effect is also considered and discussed. We find compared with the particle's shape effect, the particle diameter distribution has a much stronger impact on the particles' dispersion behavior. Thus in the simulations considered the particle's diameter distribution, the results may still be able to keep a certain accuracy while using empirical spherical particle motion model. However, in the simulations with mono-diameter particles, the particle's shape effect is obvious and shall be considered carefully.

Due to the particles' dispersion behavior is influenced by the particle's shape, we can image that this difference will influence the particle's ignitability, flammability, and the concentration of combustible gases released by the particle in the turbulent flow. In order to reveal this difference, as the first stage, in chapter five, we performed a simulation to investigate the single spheroidal particle's ignition behavior. The particle releases volatile gas and its velocity is calculated using a newly developed devolatilization model called Extended-CPD model. The volatile gas is assumed to be methane and the gas reaction is calculated by two-stage global reactions. The results are in quite well agreement with the experimental results which are published by Lee & Choi [27]. Furthermore, we find that both the diffusion and premixed regions or flames are formed around the particle. This is not revealed by the experiments in the past.

6.2 Directions for future works

This work is only a beginning of non-spherical particle motion modeling. Many fields can yet be explored. Some of the directions for further work are presented here.

Firstly, the end of this dissertation only explored the single spheroidal particle's ignition behavior. According to the conclusion of chapter three, the particle shape will affect the particles' dispersion behavior in an isotropic turbulent flow. Then we can believe that if the particles release volatile gases, the particles' dispersion will affect the gas's distribution. This means the ignitability, flammability, and the concentration of combustible gases will be influenced by the particle's shapes. How significant this influence is requires further study. A simulation of the particles dispersing in the isotropic turbulent flow and releasing volatile gases shall be performed in the future.

Secondly, the spheroidal particle model proposed in chapter two only explored and modeled the drag coefficient C_D. Although the drag force dominates the particle's motion in most cases, the lift force has a considerable effect, relatively. Hence, the lift coefficient C_L, calculated from lift force, also shall be modeled. This requires not only to extract the information of the drag force but also to extract the lift force and study the relations between the C_L and Re.

Thirdly, the spheroidal particle motion model discussed here uses a random number to determine the C_D value from the Re number. However, since the random number is generated randomly, it has no relations to the previous numbers. This means that using this model, the particle's C_D value calculated has no relations to the particle's previous states. This is a problem since the particle's motion is a continuous behavior. It will be affected by particle's previous states and will affect subsequent behavior. Thus, this model is imperfect and has to be improved in the future.

Bibliography

[1] U.S. Energy Information Administration, "International energy outlook 2016," 05 2016.

[2] BP Global, "BP Statistical Review of World Energy 2016," 06 2016.

[3] International Energy Agency, "The Impact of Global Coal Supply on Worldwide Electricity Prices," 2014.

[4] S. Elghobashi, "On predicting particle-laden turbulent flows," *Applied Scientific Research*, vol. 52, no. 4, pp. 309–329, 1994.

[5] R. Clift, J. R. Grace, and M. E. Weber, *Bubbles, Drops, and Particles*. Academic Press, 1978.

[6] A. Haider and O. Levenspiel, "Drag coefficient and terminal velocity of spherical and nonspherical particles," *Powder Technology*, vol. 58, no. 1, pp. 63 – 70, 1989.

[7] W. ZHANG, M. MUTO, K. HORI, H. WATANABE, and T. KITAGAWA, "Numerical investigation of motion of a non-spherical particle (effects of gas blowing-out on motion of a particle in a uniform flow)," *Transactions of the JSME (in Japanese)*, vol. advpub, 2015.

[8] N. Mordant and J.-F. Pinton, "Velocity measurement of a settling sphere," *The European Physical Journal B - Condensed Matter and Complex Systems*, vol. 18, no. 2, pp. 343–352, 2000.

[9] H. Watanabe and M. Otaka, "Numerical simulation of coal gasification in entrained flow coal gasifier," *Fuel*, vol. 85, no. 12-13, pp. 1935 – 1943, 2006.

[10] H. Watanabe, K. Tanno, Y. Baba, R. Kurose, and S. Komori, "Large-eddy simulation of coal combustion in a pulverized coal combustion furnace with a complex burner," *Turbulence, Heat and Mass Transfer*, vol. 6, pp. 1027–1030, 2009.

[11] R. Kurose, H. Watanabe, and H. Makino, "Numerical simulations of pulverized coal combustion," *KONA Powder and Particle Journal*, vol. 27, no. 0, pp. 144–156, 2009.

[12] M. Muto, H. Watanabe, R. Kurose, S. Komori, S. Balusamy, and S. Hochgreb, "Large-eddy simulation of pulverized coal jet flame - effect of oxygen concentration on NO_x formation," *Fuel*, vol. 142, pp. 152 – 163, 2015.

[13] N. Hashimoto and H. Watanabe, "Numerical analysis on effect of furnace scale on heat transfer mechanism of coal particles in pulverized coal combustion field," *Fuel Processing Technology*, vol. 145, pp. 20 – 30, 2016.

[14] J. F. Feng, D. D. Joseph, R. Glowinski, and T. W. Pan, "A three-dimensional computation of the force and torque on an ellipsoid settling slowly through a viscoelastic fluid," *Journal of Fluid Mechanics*, vol. 283, pp. 1–16, 01 1995.

[15] D. Broday, M. Fichman, M. Shapiro, and C. Gutfinger, "Motion of spheroidal particles in vertical shear flows," *Physics of Fluids*, vol. 10, no. 1, pp. 86–100, 1998.

[16] P. H. Mortensen, H. I. Andersson, J. J. J. Gillissen, and B. J. Boersma, "On the orientation of ellipsoidal particles in a turbulent shear flow," *International Journal of Multiphase Flow*, vol. 34, no. 7, pp. 678 – 683, 2008.

[17] J. R. Fessler, J. D. Kulick, and J. K. Eaton, "Preferential concentration of heavy particles in a turbulent channel flow," *Physics of Fluids*, vol. 6, no. 11, pp. 3742–3749, 1994.

[18] S. Chen, G. D. Doolen, R. H. Kraichnan, and Z. S. She, "On statistical correlations between velocity increments and locally averaged dissipation in homogeneous turbulence," *Physics of Fluids A*, vol. 5, no. 2, pp. 458–463, 1993.

[19] J. Jeong and F. Hussain, "On the identification of a vortex," *Journal of Fluid Mechanics*, vol. 285, pp. 69–94, 02 1995.

[20] A. Kempf, S. Wysocki, and M. Pettit, "An efficient, parallel low-storage implementation of klein's turbulence generator for LES and DNS," *Computers & Fluids*, vol. 60, pp. 58–60, 2012.

[21] N. Hashimoto, R. Kurose, H. Tsuji, and H. Shirai, "A numerical analysis of pulverized coal combustion in a multiburner furnace," *Energy & Fuels*, vol. 21, no. 4, pp. 1950–1958, 2007.

[22] D. Anthony, J. Howard, H. Hottel, and H. Meissner, "Rapid devolatilization of pulverized coal," *Symposium (International) on Combustion*, vol. 15, no. 1, pp. 1303 – 1317, 1975.

[23] D. B. Anthony and J. B. Howard, "Coal devolatilization and hydrogastification," *AIChE Journal*, vol. 22, no. 4, pp. 625–656, 1976.

[24] S. m. Hwang, R. Kurose, F. Akamatsu, H. Tsuji, H. Makino, and M. Katsuki, "Application of optical diagnostics techniques to a laboratory-scale turbulent pulverized coal flame," *Energy & Fuels*, vol. 19, no. 2, pp. 382–392, 2005.

[25] C. R. Shaddix and A. Molina, "Particle imaging of ignition and devolatilization of pulverized coal during oxy-fuel combustion," *Proceedings of the Combustion Institute*, vol. 32, no. 2, pp. 2091 – 2098, 2009.

[26] A. Molina and C. R. Shaddix, "Ignition and devolatilization of pulverized bituminous coal particles during oxygen/carbon dioxide coal combustion," *Proceedings of the Combustion Institute*, vol. 31, no. 2, pp. 1905 – 1912, 2007.

[27] H. Lee and S. Choi, "An observation of combustion behavior of a single coal particle entrained into hot gas flow," *Combustion and Flame*, vol. 162, no. 6, pp. 2610 – 2620, 2015.

[28] S. Umemoto, S. Kajitani, K. Miura, H. Watanabe, and M. Kawase, "Extension of the chemical percolation devolatilization model for predicting formation of tar compounds as soot precursor in coal gasification," *Fuel Processing Technology*, vol. 159, pp. 256 – 265, 2017.

[29] S. Niksa and A. R. Kerstein, "Flashchain theory for rapid coal devolatilization kinetics. 1. formulation," *Energy & Fuels*, vol. 5, no. 5, pp. 647–665, 1991.

[30] S. Niksa, "Flashchain theory for rapid coal devolatilization kinetics. 2. impact of operating conditions," *Energy & Fuels*, vol. 5, no. 5, pp. 665–673, 1991.

[31] P. R. Solomon, D. G. Hamblen, R. M. Carangelo, M. A. Serio, and G. V. Deshpande, "General model of coal devolatilization," *Energy & Fuels*, vol. 2, no. 4, pp. 405–422, 1988.

[32] D. M. Grant, R. J. Pugmire, T. H. Fletcher, and A. R. Kerstein, "Chemical model of coal devolatilization using percolation lattice statistics," *Energy & Fuels*, vol. 3, no. 2, pp. 175–186, 1989.

[33] T. H. Fletcher, A. R. Kerstein, R. J. Pugmire, and D. M. Grant, "Chemical percolation model for devolatilization. 2. temperature and heating rate effects on product yields," *Energy & Fuels*, vol. 4, no. 1, pp. 54–60, 1990.

[34] T. H. Fletcher, A. R. Kerstein, R. J. Pugmire, M. S. Solum, and D. M. Grant, "Chemical percolation model for devolatilization. 3. direct use of carbon-13 nmr data to predict effects of coal type," *Energy & Fuels*, vol. 6, no. 4, pp. 414–431, 1992.

[35] H. Watanabe, R. Kurose, S.-M. Hwang, and F. Akamatsu, "Characteristics of flamelets in spray flames formed in a laminar counterflow," *Combustion and Flame*, vol. 148, no. 4, pp. 234 – 248, 2007.

Acknowledgment

With the completion of this dissertation, my studying life in Japan also ended. Six years ago I came into this dreaming country for study, now with thanks to graduate. I believe this is not the end, but another hopeful start of my life, and these six years will be the most meaningful years in my life. I want to express my gratitude to all those who helped me during the study life.

Firstly, I would like to extend my sincere gratitude to my supervisor, Prof. KITAGAWA Toshiaki. Thank you for providing me such a lovely laboratory to study fluid dynamics. Without your instructive advice and useful suggestions, this dissertation could not have reached its present form.

Secondly, the sincere gratitude goes to my supervisor, Assoc. Prof. WATANABE Hiroaki. He led me into the world of science and computer simulations. He walked me through the study life from master until the doctor. He has given to me so much support, limitless patience, constant encouragement, and guidance.

I am also deeply indebted to all the other professors of the department, Prof. FURUKAWA Masato, Prof. ABE Kenichi, Assis. Prof. NAGANO Yukihide, for their constructive comments and warm encouragement to me.

Besides, I am very grateful to all the other members of the laboratory. It is a very happy time during my stay at the laboratory and throughout the process of writing this dissertation.

Last my thanks would go to my beloved family for their loving considerations and great confidence in me all through these six years. Especially thanks to my uncles and aunts, for their economy support in my studying life in Japan. And thank you, thank you for your appearance.